INTERNATIONAL JOURNAL FOR NUMERICAL METHODS IN ENGINEERING
Int. J. Numer. Meth. Engng (2015)
Published online in Wiley Online Library (wileyonlinelibrary.com). DOI: 10.1002/nme.4910

A stabilized finite element formulation for monolithic thermo-hydro-mechanical simulations at finite strain

WaiChing Sun*,†

Department of Civil Engineering and Engineering Mechanics, Columbia University in the City of New York, 614 SW Mudd, Mail Code: 4709, New York, NY 10027, USA

SUMMARY

An adaptively stabilized monolithic finite element model is proposed to simulate the fully coupled thermo-hydro-mechanical behavior of porous media undergoing large deformation. We first formulate a finite-deformation thermo-hydro-mechanics field theory for non-isothermal porous media. Projection-based stabilization procedure is derived to eliminate spurious pore pressure and temperature modes due to the lack of the two-fold inf-sup condition of the equal-order finite element. To avoid volumetric locking due to the incompressibility of solid skeleton, we introduce a modified assumed deformation gradient in the formulation for non-isothermal porous solids. Finally, numerical examples are given to demonstrate the versatility and efficiency of this thermo-hydro-mechanical model. Copyright © 2015 John Wiley & Sons, Ltd.

Received 28 July 2014; Revised 25 February 2015; Accepted 27 February 2015

KEY WORDS: thermo-hydro-mechanics; stabilized procedure; multiphysics simulations; finite strain; coupled diffusion-deformation process

1. INTRODUCTION

Thermo-hydro-mechanics (THM) is a branch of mechanics aimed to predict how deformable porous media behave, while heat transfer and fluid transport simultaneously occur in the pores filled by fluid and in the bulk of solid skeleton. Understanding these multiphysical responses is important for a wide spectrum of modern engineering applications, such as tissue scaffolding, geothermal heating, mineral exploration and mining, hydraulic fracture, and nuclear waste storage and management [1, 2]. Many of these engineering applications involve porous media undergoing substantial deformation with rapid changes on temperature and pore pressure.

In the last three decades, a considerable progress has been made for deriving mathematical theories and implementing computer models to replicate the fully coupled thermo-hydro-mechanical processes. For instance, a monolithic small-strain finite element code, FRACON, has been developed by Nguyen and Selvadurai [3]. In this code, the balance of linear momentum and mass are fully coupled, while thermal transport may affect the solid deformation and pore-fluid diffusion, but not vice versa. A generalized trapezoidal rule is used to discretize temporal space. [4] introduces a co-rotational FEM formulation and incorporate plasticity into THM model to model the non-isothermal elasto-plastic responses of porous media at large strain. In this formulation, stabilized one-point quadrature element is used to cut computational cost and avoid locking. In addition, logarithmic finite strain formulation has been derived and implemented in Karrech *et al.* [5] to overcome the aberrant oscillations encountered in large simple shear. Recent work by Preisig and Prévost

*Correspondence to: WaiChing Sun, Department of Civil Engineering and Engineering Mechanics, Columbia University in the City of New York, 614 SW Mudd, Mail Code: 4709, New York, NY 10027, USA.
†E-mail: wsun@columbia.edu

employed a fully coupled implicit THM simulator to compare the numerical solutions against the field data in a case study for carbon dioxide injection at In Salah, Algeria [6]. Kolditz *et al.* [7] introduces an open-source project OpenGeoSys, which takes advantage of an object-orient framework and provide software engineering tools such as platform-independent compiling and automated benchmarking for developers.

In addition to the monolithic finite element scheme, attempts have been made to sequentially couple multiphase flow and geomechanical simulators by establishing proper feedback and information exchange mechanisms. This strategy is often referred as operator-splitting method for which several aliases, such as fractional step, projection, and pressure correction method, exist, as pointed out by Markert *et al.* [8]. One such example is TOUGH-FLAC, which links flow simulator TOUGH2 with a small-strain finite difference code FLAC [9]. This sequential coupling approach is an attractive alternative to the monolithic approach, as it is easier to implement and maintain flow and solid simulators separately. The idea behind the operator-splitting approach is to decouple the unfavorable volume constraint from the balance of linear momentum via an immediate step. The separation of pore pressure update from the solid mechanics solver therefore provides numerical stability. In other words, proper communication must be established to ensure the correctness and numerical stability of sequential coupling schemes [6, 10–13]. The sequential coupling scheme used to link the fluid and solid simulators may have profound impact on the efficiency, stability, and accuracy of the numerical solutions. If the fluid and solid simulators use different grids or meshes, then a proper data projection scheme is required to transfer information from Gauss points and nodes of the solid mesh to the fluid mesh and vice versa [14]. For large-scale parallel simulations, the sequential couplings must be carefully designed to avoid causing bottleneck due to the difference in solver speed. This can be a significant problem if either the solid or the fluid solver runs only in serial. Recent work by Kim *et al.* [15] systematically compared fully implicit, fully explicit, semi-implicit monolithic and staggered schemes for unsaturated porous media under the isothermal condition. Numerical examples presented in Kim *et al.* [15] show that the fully implicit monolithic scheme with either inf-sup stable or stabilized equal-order finite element is advantageous on resolving sharp pore pressure gradient, but is also less efficient than the semi-implicit counterparts.

As noted in Borja [16], Mira *et al.* [17], Preisig and Prévost [6], Simoni *et al.* [18], Sun *et al.* [13], Truty and Zimmermann [19], Wan [20], White and Borja [21], and Zienkiewicz *et al.* [22], numerical stability is often a major challenge for monolithic implicit schemes that solve poromechanics models. Because of the lack of inf-sup condition [23–26], pore pressure and temperature fields may exhibit spurious oscillation patterns and/or checkerboard modes if the displacement, pore pressure, and temperature are spanned by the same set of basis function. While these spurious oscillations are less severe at the drained/isothermal limit, they may intensify when a small time step is used or when materials are near undrained/adiabatic limit. From a mathematical viewpoint, these non-physical results are due to the kernel (null space) of the discrete gradient operator being non-trivial. This non-trivial kernel makes it possible to have certain spatially oscillating pore pressure and temperature fields that have no impact on the solid deformation in a numerical simulation. To cure the numerical instability due to the lack of inf-sup condition, previous researches have established a number of techniques that employ different basis functions to interpolate displacement and pore pressure and obtain stable solutions. For instance, Zienkiewicz and coworkers [22] and Borja [27] used Taylor–Hood finite element (quadratic basis functions for displacement and linear basis function for pore pressure) to satisfy inf-sup condition and maintain numerical stability for isothermal implicit hydromechanics problems. On the other hand, Jha and Juanes [10] have shown that linear displacement combined with pore fluid velocity in the lowest-order Raviart–Thomas space, and piecewise constant pore pressure may also lead to stable solutions for isothermal poromechanics problems. Nevertheless, inf-sup stable mixed finite element models require multiple meshes for displacement, pore pressure, and/or fluid velocity. As a result, they require additional programming effort to pre-processing and post-processing data and maintain the more complex data structure.

DOI: 10.1002/nme

To avoid the complications of using multiple meshes for each solution field, an alternative is to use an equal-order finite element mesh with stabilization procedures. Many stabilization procedures have been proven to be able to eliminate the spurious oscillation modes in implicit scheme without introducing extra diffusion for small-strain isothermal poromechanics problems. For instance, White and Borja [21] employed a polynomial projection scheme originated from Dohrmann and Bochev [28] to simulate slip weakening of a fault segment. This work is extended to the large deformation regime in Sun *et al.* [13], where the stabilization term is adaptively adjusted to avoid over-diffusion. Nevertheless, to the best of the author's knowledge, stabilization procedure for finite-strain non-isothermal poromechanics has never been proposed.

The objective of this research is to fill this knowledge gap by establishing large deformation THM theory and develop the corresponding stabilized finite element model suitable for equal-order discretized displacement, pore pressure, and temperature. The resultant system of equation is solved fully implicitly and monolithically to preserve the Mandel–Cryer effect when the multiphysical coupling is strong. The necessary condition for numerical stability for THM problem and the corresponding combined inf-sup condition are derived. A new stabilization procedure is established based on the combined inf-sup condition.

The rest of the paper is organized as follows. We first establish the field theory for the THM problem in the geometrical nonlinear regime (Section 2). We then formulate the weak and Galerkin forms (Section 3.1 and 3.2) and derive stabilization techniques (Section 3.3). Based on the mass lumping technique, we suggest stabilization parameters that are large enough to eliminate spurious oscillations without over-diffusing the solution (Section 3.4). Selected benchmark and engineering application problems are simulated via the stabilized formulations (Section 4). Finally, concluding remarks are given in Section 5.

As for notations and symbols, bold-faced letters denote tensors; the symbol '$\cdot$' denotes a single contraction of adjacent indices of two tensors (e.g., $\boldsymbol{a} \cdot \boldsymbol{b} = a_i b_i$ or $\boldsymbol{c} \cdot \boldsymbol{d} = c_{ij} d_{jk}$); the symbol ':' denotes a double contraction of adjacent indices of tensor of rank two or higher (e.g., $\boldsymbol{c} : \boldsymbol{\epsilon^e} = C_{ijkl}\epsilon^e_{kl}$); the symbol '$\otimes$' denotes a juxtaposition of two vectors (e.g., $\boldsymbol{a} \otimes \boldsymbol{b} = a_i b_j$) or two symmetric second-order tensors (e.g., $(\boldsymbol{\alpha} \otimes \boldsymbol{\beta}) = \alpha_{ij}\beta_{kl}$). As for sign conventions, we consider the direction of the tensile stress and dilative pressure as positive. Throughout this paper, we employ the standard notation $H^l(\Omega), ||\cdot||_l, (\cdot,\cdot)_l, l \geq 0$, for the Sobolev spaces of all functions having square integrable derivative up to order l on a simply connected bounded domain Ω in $\mathbb{R}^3$, the corresponding Sobolev norm and inner product, respectively.

2. GOVERNING EQUATIONS AT FINITE STRAIN

In this section, we present the balance principles of mass, momentum, and energy that define the strong form of the THM problem. Following the saturated porous media theory for isothermal solid-water mixture at finite strain [13, 29, 30], we describe the kinematics of the solid skeleton with the Lagrangian coordinates while describing the motion of the pore fluid with respect to the current configuration of the solid skeleton. In addition, the following assumptions are made.

(1) Mass exchanges between solid and fluid constituents do not occur.
(2) No phase transition occurs.
(3) Pores inside the solid skeleton are fully saturated by one fluid constituent.
(4) The pore-fluid advection is negligible.
(5) The pore-fluid flow is in laminar range.
(6) No chemical reactions take place among the fluid's species.
(7) Inertial effects are negligible.
(8) The effective stress principle is valid.
(9) The temperatures of solid and fluid constituents that occupy the same material point $\boldsymbol{X} \in \mathbb{B}$ are identical.

We consider both the fluid and solid constituents compressible and that both the pore fluid and the solid skeleton may exhibit mechanical and thermal deformation.

DOI: 10.1002/nme

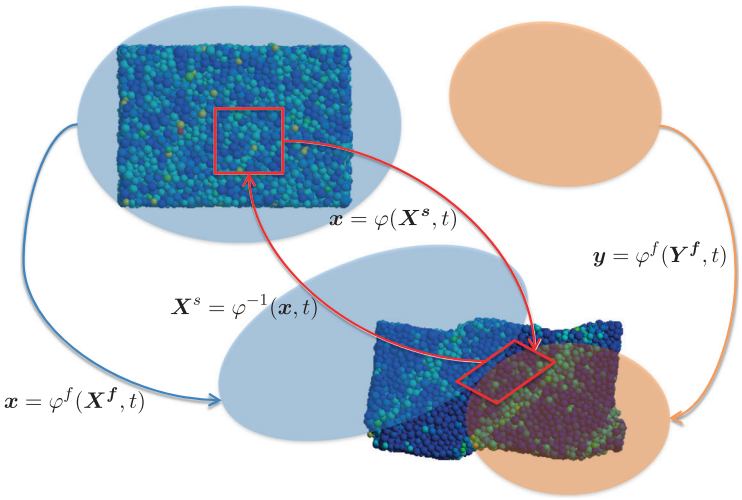

Figure 1. Trajectories of the solid and fluid constituents $\varphi^{\mathrm{s}} = \varphi$ and φ^{f}. The motion φ conserves all the mass of the solid constituent, while the fluid may enter or leave the body of the solid constituent. Figure reproduced from [13].

2.1. *Kinematics and volume fraction*

Consider a body of fully saturated porous medium $\mathcal{B}$ composed of both solid constituent and the pore fluid in the pore space, as shown in Figure 1. For a sufficiently large volume, the solid constituent and the pore fluid can be modeled as a homogenized continuum mixture. Here, we apply the continuum approach in which the solid skeleton of the body $\mathcal{B}$ is described by a set of continuously distributed points $X \in \mathcal{B}$ which occupied by a region within the Euclidean space $\mathbb{R}^3$. Notice that, except in the undrained limit, material points of pore fluid and solid skeleton do not share the same trajectory in the space–time continuum. As a result, materials at a point $\boldsymbol{x}$ of the current configuration may come from the reference configuration of the solid skeleton $\boldsymbol{X}^{\mathrm{s}}$ and/or the pore fluid counterpart $\boldsymbol{X}^{\mathrm{f}}$, that is,

$$\boldsymbol{x} = \varphi^{\alpha}(\boldsymbol{X}^{\alpha}, t) \ \alpha = \mathrm{s}, \mathrm{f}. \tag{2.1}$$

Apparently, one may choose to formulate governing equations via both mappings, φ^{s} and φ^{f}. However, because most of the constitutive laws of the solid skeleton are formulated with respect to the configurations described by φ^{s}, we formulate the finite-strain THM model with respect to the trajectory of the solid skeleton to simplify the derivations. The motion of the pore fluid is therefore taken into account by considering the relative motion between the pore fluid and the solid skeleton. For brevity, we drop the designation of the solid phase such that

$$\boldsymbol{x} = \varphi^{\mathrm{s}}(\boldsymbol{X}^{\mathrm{s}}, t) = \varphi(\boldsymbol{X}, t). \tag{2.2}$$

Therefore, the motion of the solid skeleton is described by a one-to-one mapping $\varphi : \mathcal{B} \times [0, T] \rightarrow \mathbb{R}^3$, which places a particle at the reference point $\boldsymbol{X} \in \mathcal{B}$ to a position in $\mathbb{R}^3$ in a typical time internal T. Because the solid–fluid mixture is homogenized as a continuum, the density of a fully saturated porous medium can be written as

$$\rho = \rho^{\mathrm{s}} + \rho^{\mathrm{f}} = \phi^{\mathrm{s}}\rho_{\mathrm{s}} + \phi^{\mathrm{f}}\rho_{\mathrm{f}}, \tag{2.3}$$

where $\rho_{\alpha}, \alpha = s, f$, is mass of the α constituent divided by the current volume of the α constituent, while ρ^{α} is the partial density of the α constituent, defined as the mass of the α constituent divided by the volume of the mixture in the current configuration. ϕ^{s} is the volume fraction of the solid constituent in the current configuration. ϕ^{f} is the porosity of the porous medium in the current

DOI: 10.1002/nme

configuration, which is referred as Eulerian porosity in [1]. For fully saturated porous media, $\phi^{\mathrm{s}} + \phi^{\mathrm{f}} = 1$. Thus, the total current density also reads

$$\rho = (1 - \phi^{\mathrm{f}})\rho_{\mathrm{s}} + \phi^{\mathrm{f}}\rho_{\mathrm{f}}, \tag{2.4}$$

where the densities of the solid and fluid constituents both depend on the pore pressure and the temperature.

2.2. *Balance of linear momentum*

Under the non-isothermal condition, solid skeleton may deform because of external mechanical loading, thermal expansion (or contraction), and interactions with pore-fluid. Assuming that the mixture theory is valid for porous media, we have

$$\boldsymbol{\sigma} = \boldsymbol{\sigma}^{\mathrm{s}} + \boldsymbol{\sigma}^{\mathrm{f}} = \phi^{\mathrm{s}}\boldsymbol{\sigma}_{\mathrm{s}} + \phi^{\mathrm{f}}\boldsymbol{\sigma}_{\mathrm{f}}, \tag{2.5}$$

where $\boldsymbol{\sigma}_{\mathrm{s}}$ and $\boldsymbol{\sigma}_{\mathrm{f}}$ are the intrinsic partial Cauchy stress defined in the volume of the solid grains V^{s} and pore space V^{f}, respectively. The total Cauchy stress is the volume averaged stress defined in the current volume $V = V^{\mathrm{s}} + V^{\mathrm{f}}$. Neglecting the shear resistance of the pore fluid, intrinsic partial stress of fluid consistent $\boldsymbol{\sigma}_{\mathrm{f}}$ is therefore isotropic and holds the following relation with the macroscopic pore pressure p^{f}, that is,

$$\boldsymbol{\sigma}^{\mathrm{f}} = \phi^{\mathrm{f}}\boldsymbol{\sigma}_{\mathrm{f}} = -\phi^{\mathrm{f}} p_{\mathrm{f}}\boldsymbol{I} = -p^{\mathrm{f}}\boldsymbol{I}. \tag{2.6}$$

The partial stress of the solid constituent $\boldsymbol{\sigma}_{\mathrm{s}}$ depends on the effective stress $\boldsymbol{\sigma}'$ and the stress exerted on the solid grains by the pore fluid $Kp^{\mathrm{f}}/K_{\mathrm{s}}\boldsymbol{I}$, that is,

$$\boldsymbol{\sigma}^{\mathrm{s}} = \boldsymbol{\sigma}' + \frac{K}{K_{\mathrm{s}}} p^{\mathrm{f}}\boldsymbol{I}. \tag{2.7}$$

This definition is from [31], which assumes that the non-uniform localization of stress at the grain scale, grain crushing, and damage are all insignificant to the skeleton (cf. [22, p.8–11]). By substituting (2.6) and (2.7) into (2.5), the total Cauchy stress now reads

$$\boldsymbol{\sigma} = \boldsymbol{\sigma}' - Bp^{\mathrm{f}}\boldsymbol{I}, \tag{2.8}$$

where B is the Biot's coefficient defined as [31]

$$B = 1 - \frac{K}{K_{\mathrm{s}}}. \tag{2.9}$$

Typically, Biot's coefficient B is close to unity for sand, but can be ranged from 0.5 to 0.8 for rocks or concrete. Notice that B in (2.8) have been defined in a number of different ways in the literature. For instance, Terzaghi and Rendulic [32] defined B as a function of the effective area of solid grains [33]. For bio-materials and composites, Cowin and Doty [34] generalize the effective stress concept in [35] and introduce the effective stress coefficient tensor $\boldsymbol{B}$, that is,

$$\boldsymbol{\sigma} = \boldsymbol{\sigma}' - p^{\mathrm{f}}\boldsymbol{B}. \tag{2.10}$$

This definition of effective stress is not adopted in this work, but will be considered in future study. The balance of linear momentum therefore reads,

$$\nabla^{\boldsymbol{x}}\cdot\boldsymbol{\sigma} + \rho\boldsymbol{G} + \boldsymbol{h}^{\mathrm{s}} + \boldsymbol{h}^{\mathrm{f}} = \boldsymbol{0}, \tag{2.11}$$

where $\boldsymbol{G}$ is the acceleration due to gravity. $\boldsymbol{h}^{\mathrm{s}}$ and $\boldsymbol{h}^{\mathrm{f}}$ are the interactive body forces per unit reference volume exerted on their corresponding phases due to drag, lift, virtual mass effect, history effects, and the relative spinning (Magnus effect), which balance out internally, that is, $\boldsymbol{h}^{\mathrm{s}} + \boldsymbol{h}^{\mathrm{f}} = \boldsymbol{0}$ [36]. In the total Lagrangian formulation, balance of linear momentum in Equation (2.11) is rewritten in reference configuration via the Piola transformation [37], that is,

$$\nabla^{\boldsymbol{X}}\cdot\boldsymbol{P} + J\rho\boldsymbol{G} = \boldsymbol{0}, \tag{2.12}$$

DOI: 10.1002/nme

where $\boldsymbol{P}$ denotes the total first Piola–Kirchhoff stress and $J = \det(\boldsymbol{F})$ is the determinant of the deformation gradient of the solid skeleton $\boldsymbol{F}$. Similar to the total Cauchy stress, the total first Piola–Kirchhoff stress can be partitioned into two parts, the effective first Piola–Kirchhoff stress $\boldsymbol{P}'$ and the pull-back of the pore fluid contribution $JBp^{\mathrm{f}}\boldsymbol{F}^{-T}$. The effective first Piola–Kirchhoff stress $\boldsymbol{P}'$ is the amount of stress carried by the solid skeleton. For solid skeleton exhibiting elasto-plastic responses, the effective first Piola–Kirchhoff stress can be determined from the deformation gradient and the internal variable(s) z of the solid skeleton,

$$\boldsymbol{P}(\boldsymbol{F}, z, p^f, \theta) = \boldsymbol{P'}(\boldsymbol{F}, z, \theta) - JBp^f \boldsymbol{F}^{-T}. \tag{2.13}$$

Under the non-isothermal condition, the multiplicative decomposition of the deformation gradient can be written as [37]

$$\boldsymbol{F} = \frac{\partial \boldsymbol{\varphi}(\boldsymbol{X}, t)}{\partial \boldsymbol{X}} = \boldsymbol{F}_M \cdot \boldsymbol{F}_\theta \ ; \ \boldsymbol{F}_\theta = \frac{\partial \boldsymbol{\varphi}_\theta(\boldsymbol{X}, t)}{\partial \boldsymbol{X}} \ ; \boldsymbol{F}_M = \frac{\partial \boldsymbol{\varphi}_M(\boldsymbol{X}_\theta, t)}{\partial \boldsymbol{X}_\theta}, \tag{2.14}$$

where $\boldsymbol{F}_\theta$ and $\boldsymbol{F}_M$ are the pure thermal and mechanical splits of the deformation gradient.

As shown in Figure 2, the mechanical split $\boldsymbol{F}_M$ of the deformation gradient can be further decomposed into the elastic and plastic parts such that

$$\boldsymbol{F}_M = \boldsymbol{F} \cdot \boldsymbol{F}_\theta^{-1} = \boldsymbol{F}^e \cdot \boldsymbol{F}^p \ ; \ \boldsymbol{F}^p = \frac{\partial \boldsymbol{\varphi}^p(\boldsymbol{X}_\theta, t)}{\partial \boldsymbol{X}_\theta} \ ; \ \boldsymbol{F}^e = \frac{\partial \boldsymbol{\varphi}^e(\boldsymbol{X}_{\boldsymbol{\sigma}'=\boldsymbol{0}}, t)}{\partial \boldsymbol{X}_{\boldsymbol{\sigma}'=\boldsymbol{0}}}, \tag{2.15}$$

where $\boldsymbol{\varphi}_\theta(\mathcal{B})$ is the intermediate thermal effective-stress-free configuration caused by thermal expansion or contraction. Similarly, $\boldsymbol{\varphi}^p(\boldsymbol{\varphi}_\theta(\mathcal{B}))$ is the intermediate effective-stress-free configuration, which can be obtained by deforming the current configuration via $\boldsymbol{\varphi}^{e-1}$. Notice that we do not consider the possibility of having the pore pressure split for the deformation gradient of the solid skeleton. In addition, we assume that the thermal expansion is isotropic. To replicate the thermal effect accurately, anisotropy of thermal effect must be considered for composite or reinforced materials. Nevertheless, anisotropy of thermal conductivity is often neglected in the literature, partly because of the lack of data to characterize detailed tensorial thermal conductivity in field and experimental settings. As a result, $\boldsymbol{F}_\theta$ can be characterized by the thermal expansion coefficient $\alpha_{\mathrm{sk}}(\theta)$, that is,

$$\boldsymbol{F}_\theta = \exp\left[\int_{\hat{\theta}}^{\theta} \alpha_{\mathrm{sk}}(\hat{\theta}) d\hat{\theta}\right] \boldsymbol{I}. \tag{2.16}$$

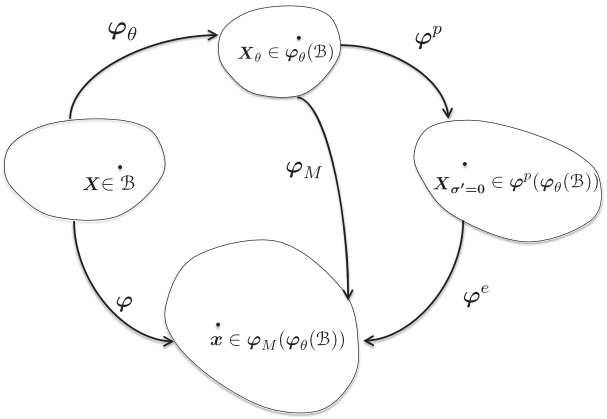

Figure 2. Multiplicative decomposition of the thermo-hydro-mechanics deformation.

DOI: 10.1002/nme

If the thermal expansion coefficient is constant, then we have

$$\boldsymbol{F}_\theta = \exp[\alpha_{\mathrm{sk}}(\theta-\theta_o)]\boldsymbol{I} \;;\; J_\theta = \exp[3\alpha_{\mathrm{sk}}(\theta-\theta_o)], \tag{2.17}$$

where θ_o is the reference temperature at which there is no thermal-induced deformation. Notice that linearizing the thermal expansion defined in (2.17) leads to the classical thermal strain $\epsilon_v = \log J_\theta = 3\alpha_{\mathrm{sk}}(\theta-\theta_o)$. Recall that the configuration $\boldsymbol{\varphi}_\theta(\mathcal{B})$ is stress free, and the thermal-induced deformation gradient is isotropic, thus, $\boldsymbol{F} = \boldsymbol{F}_\theta\boldsymbol{F}_M = \boldsymbol{F}_M\boldsymbol{F}_\theta$. As a result, Equation (2.13) can be rewritten as

$$\boldsymbol{P}\left(\boldsymbol{F}_M, z, p^f\right) = \boldsymbol{P'}(\boldsymbol{F}_M, z) - JBp^f\boldsymbol{F}^{-T}, \tag{2.18}$$

in which the thermal expansion alone does not induce any change in the effective stress of the solid skeleton.

2.3. Balance of fluid content

The three-dimensional balance of fluid content equation for fully saturated porous media was first derived by Biot [35]. Rice and Cleary [38] extended this study by taking account of the compressibility of fluid and solid constituents, and provided analytical solution for pressurized cylindrical and spherical cavity under the isothermal condition. This version of balance of fluid content was then further generalized by McTigue [2] who takes account of the thermal coupling effect of fluid-saturated porous media in the geometrical linear regime. In this study, our new contribution is to provide the derivations for the balance of fluid mass in the geometrical nonlinear regime. In particular, we adopt the notations of Eulerian and Lagrangian porosities introduced by Coussy [1]. Using this as a starting point, we derive the balance of fluid content equation of the non-isothermal porous media in the reference configuration.

Let us first define the Lagrangian fluid content $M^{\mathrm{f}} : \mathcal{B}\times[0,T] \to \mathbb{R}^+$ as the fluid mass per unit reference volume. The fluid content is therefore a function of the porosity and the fluid density, that is,

$$M^{\mathrm{f}} = J\rho^{\mathrm{f}} = J\phi^{\mathrm{f}}\rho_{\mathrm{f}} = \Phi^{\mathrm{f}}\rho_{\mathrm{f}}, \tag{2.19}$$

where $\Phi^{\mathrm{f}}(\boldsymbol{X},t) = J(\boldsymbol{X},t)\phi^{\mathrm{f}}(\boldsymbol{\varphi}(\boldsymbol{X},t),t)$ is the Lagrangian porosity, the ratio between current void volume to the initial total volume (cf. [1, p. 5]). In the current configuration, the balance of fluid mass content reads, that is,

$$\frac{D}{Dt}\int_{\boldsymbol{\varphi}(\mathcal{B})}\phi^{\mathrm{f}}\rho_{\mathrm{f}}dv = -\int_{\partial\boldsymbol{\varphi}(\mathcal{B})}\boldsymbol{w}\cdot\boldsymbol{n}\,da. \tag{2.20}$$

Applying Reynold's transport theorem and Gauss's theorem, we obtain the corresponding local fluid content continuity equation in the current configuration

$$\frac{DJ\phi^{\mathrm{f}}\rho_{\mathrm{f}}}{Dt} + J\nabla^{\boldsymbol{x}}\cdot\boldsymbol{w} = 0, \tag{2.21}$$

where $D\phi^{\mathrm{f}}\rho_f/Dt$ is the material time derivative of the current fluid density that reads,

$$\frac{DJ\phi^{\mathrm{f}}\rho_f}{Dt} = \frac{\partial J\phi^{\mathrm{f}}\rho_{\mathrm{f}}}{\partial t} + \phi^{\mathrm{f}}\rho_{\mathrm{f}}\dot{J}, \tag{2.22}$$

where $\dot{(\cdot)} = D(\cdot)/Dt$. In (2.20) and (2.21), $\boldsymbol{w}$ is the relative pore-fluid mass flux in the deforming solid skeleton body. Assuming that the pore-fluid flow is Darcian, then the relative pore-fluid mass flux is related to both the gradient of the pore pressure and the temperature under non-isothermal condition, that is,

$$\boldsymbol{w} = \rho_{\mathrm{f}}\boldsymbol{k}\cdot\left[-\nabla^{\boldsymbol{x}}p^{\mathrm{f}} + \rho_{\mathrm{f}}\boldsymbol{G}\right] - \rho_{\mathrm{f}}s_T\nabla^{\boldsymbol{x}}\theta, \tag{2.23}$$

DOI: 10.1002/nme

where $\boldsymbol{k}$ is the permeability tensor divided by the viscosity; S_T is the Soret coefficient. In particular, the latter term $s_T \nabla^{\boldsymbol{x}} \cdot \theta$ represents a phenomenon analogous to the Ludwig–Soret effect (the flux induced by the gradient of temperature) [2, 39, 40].

The balance of mass content in the Lagrangian configuration can be obtained from (2.21) via Piola transformation, that is,

$$\frac{DM^{\mathrm{f}}}{Dt} = -\nabla^{\boldsymbol{X}} \cdot \boldsymbol{W}. \tag{2.24}$$

The Lagrangian relative mass flux $\boldsymbol{W}$ can be obtained via the Piola identity, that is,

$$\boldsymbol{W} = J\boldsymbol{F}^{-1} \cdot \boldsymbol{w}. \tag{2.25}$$

Furthermore, let us assume that the inertial force is negligible, $\boldsymbol{a}^f = \boldsymbol{0}$. After a pull-back operation, the Lagrangian mass flux reads

$$\boldsymbol{W} = \rho_{\mathrm{f}} \boldsymbol{Q}_{\mathrm{f}} = \rho_{\mathrm{f}} \boldsymbol{k} \cdot \left(-\nabla^{\boldsymbol{X}} p^{\mathrm{f}} + \rho_{\mathrm{f}} \boldsymbol{F}^{\mathrm{T}} \cdot \boldsymbol{G} \right) - \rho_{\mathrm{f}} \boldsymbol{S}_T \nabla^{\boldsymbol{x}} \theta, \tag{2.26}$$

where both the permeability tensor and Soret coefficient tensor are both positive semi-definite, that is,

$$\boldsymbol{k} = J\boldsymbol{F}^{-1} \cdot \boldsymbol{k} \cdot \boldsymbol{F}^{-\mathrm{T}} \; ; \; \boldsymbol{S}_T = J s_T \boldsymbol{C}^{-1}, \tag{2.27}$$

where $\boldsymbol{C} = \boldsymbol{F}^{\mathrm{T}} \cdot \boldsymbol{F}$ is the right Cauchy–Green tensor. Next, we consider the local rate of change of the fluid content M^{f} in the left-hand side of (2.24). The material time derivative of the fluid mass content can be partitioned by applying the chain rule on (2.19),

$$\dot{M}^{\mathrm{f}} = \Phi^{\mathrm{f}} \dot{\rho}_{\mathrm{f}} + \rho_{\mathrm{f}} \dot{\Phi}^{\mathrm{f}}. \tag{2.28}$$

To complete the formulation, we need to re-express (2.28) in terms of the two fields $\boldsymbol{\varphi}$ and p^{f}. As a result, we assume that the pore fluid density only depends on temperature θ and pore pressure p^{f}. Hence, we have

$$\dot{\rho}_{\mathrm{f}} \left(\theta, p^{\mathrm{f}} \right) = \left. \frac{\partial \rho_{\mathrm{f}}}{\partial p^{\mathrm{f}}} \right|_{\theta} \dot{p}^{\mathrm{f}} + \left. \frac{\partial \rho_{\mathrm{f}}}{\partial \theta} \right|_{p^{\mathrm{f}}} \dot{\theta}. \tag{2.29}$$

In the preceding expression, $\partial \rho^{\mathrm{f}} / \partial p^{\mathrm{f}}|_{\theta}$ represents the change of the density due to pore pressure rise/drop at a fixed temperature, while $\partial \rho^{\mathrm{f}} / \partial \theta|_{p^{\mathrm{f}}}$ represents the change of density due to a temperature rise/drop at a fixed pore pressure. Assuming that the bulk modulus K_{f} and thermal expansion coefficient α_{f} of the pore fluid remains constant, we have

$$\rho_{\mathrm{f}}(\theta, p^{\mathrm{f}}) = \rho_{\mathrm{f}o} \exp \left(\frac{p^{\mathrm{f}} - p^{\mathrm{f}}_o}{K_{\mathrm{f}}} - 3\alpha_{\mathrm{f}}(\theta - \theta_o) \right). \tag{2.30}$$

Hence, $\partial \rho^{\mathrm{f}} / \partial p^{\mathrm{f}}|_{\theta}$ and $\partial \rho^{\mathrm{f}} / \partial \theta|^{\mathrm{f}}_{p}$ can be written as

$$\left. \frac{\partial \rho_{\mathrm{f}}}{\partial p^{\mathrm{f}}} \right|_{\theta} = \frac{\rho_{\mathrm{f}}}{K_{\mathrm{f}}} \; ; \; \left. \frac{\partial \rho_{\mathrm{f}}}{\partial \theta} \right|_{p^{\mathrm{f}}} = -3\rho_{\mathrm{f}} \alpha_{\mathrm{f}}. \tag{2.31}$$

Meanwhile, the constitutive relation of the Lagrangian porosity Φ^{f} is a function of $\boldsymbol{\varphi}$, p^{f}, and θ. For example, one may generalize Athy's exponential porosity–pressure relation [41] and express the Lagrangian porosity as shown in (2.32).

$$\Phi^{\mathrm{f}} = \Phi^{\mathrm{f}}_o \exp \left(B \log J + \frac{B - \Phi^{\mathrm{f}}}{K_{\mathrm{s}}} (p^{\mathrm{f}} - p^{\mathrm{f}}_o) - 3(J - \Phi^{\mathrm{f}}) \alpha_{\mathrm{s}} (\theta - \theta_o) \right), \tag{2.32}$$

DOI: 10.1002/nme

where $\log J = \log(\det \boldsymbol{F}) = \mathrm{tr}\boldsymbol{\epsilon}$, $\boldsymbol{\epsilon}$ is the Eulerian logarithm strain tensor, and α_s is the thermal expansion coefficient of the solid constituent. This version of porosity constitutive law features a multiplicative decomposition which reads

$$\Phi^\mathrm{f} = J^{\boldsymbol{\varphi}} J^{p^\mathrm{f}} J^{\theta} \Phi^\mathrm{f}_o, \tag{2.33}$$

where

$$J^{\boldsymbol{\varphi}} = \exp(B \log J);\ J^{p^\mathrm{f}} = \exp\left(\frac{B-\Phi^\mathrm{f}}{K_\mathrm{s}}\left(p^\mathrm{f} - p^\mathrm{f}_o\right)\right);\ J^{\theta} = \exp(-3(J-\Phi^\mathrm{f})\alpha_\mathrm{s}(\theta-\theta_o)). \tag{2.34}$$

The advantage of a constitutive law like (2.32) is that it will not predict an unphysical negative porosity even under extreme loading conditions. However, as argued by Armero in [29] and subsequently in [5, 42], it is more consistent with the nature of the fluid content, a scalar field, to be modeled by additive decompositions in both infinitesimal [1] and finite deformation regimes [29, 42]. Because for porous media with incompressible fluid constituents, $\dot{M}^\mathrm{f} = \rho_\mathrm{f}\dot{\Phi}^f$, an additive decomposition of fluid content implies that the Lagrangian porosity should also be defined in an additive decomposition. As a result, we employ a linear approximation of (2.32), that is,

$$\Phi^\mathrm{f} - \Phi^\mathrm{f}_o \approx \log J^{\boldsymbol{\varphi}} + \log J^{p^\mathrm{f}} + \log J^{\theta} = B\,\log J + \frac{B-\Phi^\mathrm{f}}{K_\mathrm{s}}(p^\mathrm{f} - p^\mathrm{f}_o) - 3\left(J-\Phi^\mathrm{f}\right)\alpha_s(\theta-\theta_o). \tag{2.35}$$

Equation (2.35) is identical to the Lagrangian porosity defined in [1, 43] if the thermal coefficient term in [1, 43] $\alpha_\phi = \Phi^s\alpha_\mathrm{s} = (J-\Phi^f)\alpha_\mathrm{s}$. Taking the material time derivative of (2.35), the material time derivative of Lagrangian porosity now reads

$$\dot{\Phi}^\mathrm{f} = \frac{\partial\Phi^\mathrm{f}}{\partial J}\Big|_{(p^\mathrm{f},\theta)}\dot{J} + \frac{\partial\Phi^\mathrm{f}}{\partial p^\mathrm{f}}\Big|_{(\boldsymbol{\varphi},\theta)}\dot{p}^\mathrm{f} + \frac{\partial\Phi^\mathrm{f}}{\partial\theta}\Big|_{(\boldsymbol{\varphi},p^\mathrm{f})}\dot{\theta}. \tag{2.36}$$

Assuming that B and K_s remain constant and taking the material time derivative of (2.35) leads to,

$$\left(1 + \frac{p^\mathrm{f}-p^\mathrm{f}_o}{K_\mathrm{s}} - 3\alpha_s(\theta-\theta_o)\right)\dot{\Phi}^\mathrm{f} = \frac{B}{J}\dot{J} - 3\alpha_\mathrm{s}(\theta-\theta_o)\dot{J} + \frac{B-\Phi^\mathrm{f}}{K_\mathrm{s}}\dot{p}^\mathrm{f} - 3(J-\Phi^\mathrm{f})\alpha_\mathrm{s}\dot{\theta}. \tag{2.37}$$

For simplicity, let $|p^\mathrm{f}| << K_s$ and $|\alpha_\mathrm{s}(\theta-\theta_o)| << 1$. Substituting (2.29), (2.31), and (2.37) into (2.28) and working through algebra, we obtain the expression of the material time derivative of the fluid content $\dot{M}^\mathrm{f}$, which reads

$$\dot{M}^\mathrm{f} = \rho_\mathrm{f}\left(\left(\frac{B}{J} - 3\alpha_\mathrm{s}(\theta-\theta_o)\right)\dot{J} + \frac{1}{M}\dot{p}^\mathrm{f} - 3\alpha^\mathrm{m}\dot{\theta}\right), \tag{2.38}$$

where M is the Biot's modulus as defined in [1, 31]. α^m is the thermal expansion coefficient of the mixture. In infinitesimal range where $\Phi^\mathrm{f} \approx \phi^\mathrm{f}$, this definition is identical to the thermal expansion coefficient in [6], that is,

$$M = \frac{K_\mathrm{s}K_\mathrm{f}}{K_f(B-\Phi^\mathrm{f}) + K_\mathrm{s}\Phi^\mathrm{f}}\ ;\ \alpha^\mathrm{m} = \Phi^\mathrm{s}\alpha_\mathrm{s} + \Phi^\mathrm{f}\alpha_\mathrm{f} = (J-\Phi^\mathrm{f})\alpha_\mathrm{s} + \Phi^\mathrm{f}\alpha_\mathrm{f}. \tag{2.39}$$

Combining (2.26) and (2.38), we obtain the strong form of the balance of fluid content equation,

$$\left(\frac{B}{J} - 3\alpha_\mathrm{s}(\theta-\theta_o)\right)\dot{J} + \frac{1}{M}\dot{p}^\mathrm{f} - 3\alpha^\mathrm{m}\dot{\theta} + \frac{1}{\rho_\mathrm{f}}\nabla^{\boldsymbol{X}}\cdot\boldsymbol{W} = 0. \tag{2.40}$$

Notice that if both constituents are incompressible, then $B = 1, 1/M = 0$, and $\nabla^{\boldsymbol{x}}\rho_\mathrm{f} = 0$. Applying the Piola transform and assuming isothermal condition, (2.40) reduces to the form identical to that seen in [30],

DOI: 10.1002/nme

$$\nabla^{\boldsymbol{x}} \cdot \boldsymbol{v} + \nabla^{\boldsymbol{x}} \cdot \boldsymbol{q} = 0, \tag{2.41}$$

where $\boldsymbol{q} = (1/\rho_f)\boldsymbol{w}$. In summary, the balance law expressed in (2.40) captures the influence of the skeleton deformation and heat transfer on fluid transport in the following ways.

(1) Compression or expansion of fluid induced by solid skeleton deformation.
(2) Shrinkage or expansion of the pore space that leads to the change of the change of specific storage.
(3) Expansion or shrinkage of solid and fluid constituents due to temperature changes.
(4) The Soret effect, that is, the thermo-induced diffusion of pore fluid.
(5) The geometrical nonlinear effect due to the deformation of solid skeleton.

Remark 1
One important observation of the derivation shown in (2.32)–(2.40) is that both the balance of energy and the balance of fluid content equations depend strongly on the porosity evolution law in the geometrically nonlinear regime.

2.4. Balance of energy

In the vast body of literature on THM problems, the expression of balance of energy differs significantly because of the variety of underlying assumptions. For the sake of simplification, some THM models assume that both the skeleton deformation and pore-flow diffusion processes impose negligible influences on the heat transfer process and thus lead to a decoupled heat transfer equation in the infinitesimal regime [2, 3, 44, 45], that is,

$$\nabla^{\boldsymbol{x}} k_\theta \nabla^{\boldsymbol{x}} \theta = \rho C_p \dot{\theta}, \tag{2.42}$$

where k_θ and C_p are the volume averaged thermal conductivity and heat capacity of the fluid–solid mixture. Similar assumptions are made in several other small-strain THM codes reported in international co-operative research project DECOVALEX [46] and in the open source simulation code OpenGeoSys [7].

Our objective here is to provide a more complete energy balance law to bring new sights on the thermo-hydro-mechanical responses of porous media. In particular, we consider the contribution of the mechanical work done by the solid skeleton and pore-fluid, the density variation, and size changes of pore space due to thermo-hydro-mechanical coupling and the geometrical nonlinear effect in finite strain regime. To simplify the derivation, we consider that all phases of the saturated porous media are locally in thermal equilibrium, and hence the temperature of both solid and fluid constituents are identical locally (in a homogenized sense of each elementary representative volume), that is, $\theta_s = \theta_f = \theta$. Except the additional advection term, the local balance of energy is in analogous to that of the single-phase thermo-plasticity materials [47],

$$c_{\boldsymbol{F}} \dot{\theta} = [D_{\text{mech}} - H_\theta] + \left[-J \nabla^{\boldsymbol{x}} q_\theta + \frac{\phi^{\text{f}} c_{\boldsymbol{F}\text{f}}}{\rho_{\text{f}}} J \boldsymbol{w} \cdot \nabla^{\boldsymbol{x}} \theta + R_\theta \right], \tag{2.43}$$

where $c_{\boldsymbol{F}}$ is the specific heat capacity per unit volume of the porous media *at constant deformation* [37]. For the fully saturated, two-phase porous media, the specific heat capacity of the solid–fluid mixture can be obtained by volume averaging the specific heat capacities of the solid and fluid constituents, that is,

$$c_{\boldsymbol{F}} = (J - \Phi^{\text{s}}) c_{\boldsymbol{F}\text{s}} + \Phi^{\text{f}} c_{\boldsymbol{F}\text{f}} = (J - \Phi^{\text{s}}) \rho_{\text{fo}} c_{\text{s}} + \Phi^{\text{f}} \rho_{so} c_{\text{f}}, \tag{2.44}$$

where ρ_{fo} and ρ_{so} are the initial densities, and c_{f} and c_{s} are the specific heat capacities (per unit mass) of the fluid and solid constituents. D_{mech} denotes the contribution to the dissipation due to pure mechanical load. On the other hand, H_θ is the non-dissipative (latent) structural heating or cooling [37]. At the adiabatic limit without heat source, the last three terms in (2.43) can be neglected. By contrary, for many petroleum and geotechnical engineering applications, the life cycle of the

DOI: 10.1002/nme

thermo-hydro-mechanical system is in the order of years. For those applications, it is common to neglect the contribution from the structural heating and dissipation as shown in [2–4, 7, 9, 18, 45, 48].

Here, we assume that the structural heating is thermoelastic. This leads to the classical Gough–Joule coupling effect in which local temperature changes may occur when a porous medium undergoes adiabatic deformation. R_θ is the heat source term. $-J\nabla(q_\theta/J)$ is the heat conduction term. Pulling back (2.43) into the reference configuration via the Piola transformation yields

$$c_{\boldsymbol{F}}\dot{\theta} = [D_{\text{mech}} - H_\theta] + \left[-\nabla^{\boldsymbol{X}}\cdot\boldsymbol{Q}_\theta + \frac{\Phi^{\text{f}}c_{\boldsymbol{F}^{\text{f}}}}{\rho_{\text{f}}}\boldsymbol{W}\cdot\boldsymbol{F}^{-T}\nabla^{\boldsymbol{X}}\theta + R_\theta\right], \tag{2.45}$$

where Q_θ is the Piola–Kirchhoff heat flux. Assuming that both the solid and fluid constituents obey Fourier's law, the Cauchy heat flux is often written as the dot product of the volume averaged heat conductivity tensor and the gradient of temperature [49], that is,

$$q_\theta = \phi^{\text{f}}\boldsymbol{k}_\theta^{\text{f}}\nabla^{\boldsymbol{x}}\theta + (1-\phi^{\text{f}})\boldsymbol{k}_\theta^{\text{s}}\nabla^{\boldsymbol{x}}\theta = \boldsymbol{k}_\theta\nabla^{\boldsymbol{x}}\theta, \tag{2.46}$$

where $\boldsymbol{k}_\theta = \phi^{\text{f}}\boldsymbol{k}_\theta^{\text{f}} + (1-\phi^{\text{f}})\boldsymbol{k}_\theta^{\text{s}}$ is the volume averaged heat conductivity tensor. However, this volume averaged approach is only valid if the solid and fluid constituents are connected in parallel. Presumably, calculating the correct homogenized effective heat conductivity requires knowledge of the pore geometry and connectivity, which can be obtained from three-dimensional tomographic images [50, 51] or directly from experiments. However, because micro-structural attributes of pore space is not always available, we adopt an alternative homogenization approach where equivalent inclusion method is used to determine effective heat conductivity tensor of the two-phase materials [52]. Assuming that the pore fluid as the bulk material and the solid grains as spherical inclusions, the effective thermal conductivity may be estimated via Eshelby equivalent inclusion method reads

$$\boldsymbol{k}_\theta = \left(k_\theta^f + \frac{\left(1-\phi^{\text{f}}\right)\left(k_\theta^{\text{s}}-k_\theta^{\text{f}}\right)k_\theta^{\text{f}}}{\left(k_\theta^{\text{s}}-k_\theta^{\text{f}}\right)\phi^{\text{f}}+k_\theta^{\text{f}}}\right)\boldsymbol{I} = \left(k_\theta^f + \frac{\left(J-\Phi^{\text{f}}\right)\left(k_\theta^{\text{s}}-k_\theta^{\text{f}}\right)k_\theta^{\text{f}}}{\left(k_\theta^{\text{s}}-k_\theta^{\text{f}}\right)\Phi^{\text{f}}+Jk_\theta^{\text{f}}}\right)\boldsymbol{I}, \tag{2.47}$$

where k_θ^{s} and k_θ^{f} are the isotropic thermal conductivity coefficient of the solid and the fluid constituents. Applying the Piola transformation and using the relations $\Phi^{\text{s}}+\Phi^{\text{f}} = J$ and $\phi^{\text{s}}+\phi^{\text{f}} = 1$, (2.46) can be rewritten in reference configuration, that is,

$$J^{-1}\boldsymbol{F}\,Q_\theta = -\boldsymbol{k}_\theta\boldsymbol{F}^{-T}\nabla^{\boldsymbol{X}}\theta\,. \tag{2.48}$$

Hence, the Piola–Kirchhoff heat flux Q_θ corresponding to (2.46) reads

$$Q_\theta = -K_\theta\nabla^{\boldsymbol{X}}\theta, \tag{2.49}$$

where K_θ is the pull-back thermal conductivity tensor, that is,

$$\boldsymbol{k}_\theta = J\boldsymbol{F}^{-1}\cdot\boldsymbol{k}_{\boldsymbol{\theta}}\cdot\boldsymbol{F}^{-T}. \tag{2.50}$$

2.4.1. Simplified heat transfer equation in the geometrically nonlinear regime. If both the mechanical dissipation and the Gough–Joule coupling effect are neglected, then we recover the finite deformation version of the heat transfer equation in [3, 7, 44, 45, 48], which reads

$$c_{\boldsymbol{F}}\dot{\theta} - \nabla^{\boldsymbol{X}}\cdot\boldsymbol{k}_\theta\nabla^{\boldsymbol{X}}\theta + \frac{\Phi^{\text{f}}c_{\boldsymbol{F}^{\text{f}}}}{\rho_{\text{f}}}\boldsymbol{W}\cdot\boldsymbol{F}^{-T}\cdot\nabla^{\boldsymbol{X}}\theta - R_\theta = 0. \tag{2.51}$$

Notice that the thermal diffusion process is fully coupled with the skeleton deformation in the geometrical non-linear regime, even if the mechanical dissipation and Gough–Joule coupling effect are both neglected. This coupling effect is captured by the porosity changes and volumetric deformation that lead to changes in the effective specific heat $C_{\boldsymbol{F}}$, the pull-back conductivity tensor, and the convection term. If the both structural heat and dissipation mechanisms exhibit little influence

DOI: 10.1002/nme

on the thermal diffusion process of the porous medium, then (2.51) is sufficient. However, for more general cases, particularly biological tissues or other rubber-like materials, both the structural heat and dissipation mechanism must be taken into account properly.

2.4.2. Structural heating and the Gough–Joule coupling effect. Giving the fact that the actual expressions of both structural heating and dissipation vary significantly for different material models, we consider Equation (2.45), a general statement for the energy conservation law. However, we may introduce additional assumptions to express the balance of energy in a more explicit form. For instance, we may assume that the structural heating contains no latent plastic terms, and this is identical with the thermoelastic heating [47]. To further particularize the problem, assume that the non-dissipative (latent) structural heating or cooling H_θ is the sum of the power contributed by the solid skeleton and the pore fluid, that is,

$$H_\theta = H_\theta^{\mathrm{s}} + H_\theta^{\mathrm{f}}, \tag{2.52}$$

where power contributed by the volumetric deformation of the solid skeleton reads [47]

$$H_\theta^{\mathrm{s}} = -\theta \frac{\partial}{\partial \theta} \boldsymbol{P'} : \dot{\boldsymbol{F}} = -\theta \frac{\partial^2}{\partial J \, \partial \theta} 3\alpha_{\mathrm{sk}} K \log J(\theta - \theta_o)\dot{J} = -3K\alpha_{sk}\theta \frac{\dot{J}}{J}. \tag{2.53}$$

Following the derivation in [1], the pore-fluid contribution reads

$$H_\theta^{\mathrm{f}} = -\theta \frac{\partial}{\partial \theta} 3\alpha^{\mathrm{m}}(\theta - \theta_o)\dot{p^{\mathrm{f}}} = -3\alpha^{\mathrm{m}}\theta \dot{p^{\mathrm{f}}}. \tag{2.54}$$

Substituting (2.53) and (2.54) into (2.45) and neglect the mechanical dissipation, we obtain the energy balance equation that takes account of the Gough–Joule coupling effect,

$$c_{\boldsymbol{F}}\dot{\theta} - 3K\alpha_{sk}\theta\frac{\dot{J}}{J} - 3\alpha^{\mathrm{m}}\theta\dot{p^{\mathrm{f}}} - \nabla^{\boldsymbol{X}} \cdot \boldsymbol{k}_\theta \nabla^{\boldsymbol{X}}\theta + \frac{\Phi^{\mathrm{f}} c_{\boldsymbol{F}^{\mathrm{f}}}}{\rho_{\mathrm{f}}} \boldsymbol{W} \cdot \boldsymbol{F}^{-T} \cdot \nabla^{\boldsymbol{X}}\theta - R_\theta = 0. \tag{2.55}$$

3. STABILIZED VARIATIONAL FORMULATION

In this section, we consider the stabilized variational form for the equal-order displacement–pressure–temperature finite element model, with assumed deformation gradient that prevents volumetric locking. We first define the standard weak form of the poromechanics problem based on the balance law derived in Section 2. By applying a multiplicative split, we introduce the assumed deformation gradient for the THM problem. To prevent spurious modes due to the usage of equal-order interpolations, we introduce a stabilization mechanism into the weighted-residual statement of the mass and energy balance equations. A simple scheme for choosing the stabilization parameters is also presented.

3.1. Galerkin form

Our objective is to derive a weighted-residual statement suitable for a total Lagrangian scheme. We first specify the appropriate boundary and initial conditions. Following the standard line, we consider a domain $\mathcal{B}$ whose boundary $\partial\mathcal{B}$ is the direct sum of the Dirichlet and von Neumann boundaries, that is,

$$\partial\mathcal{B} = \overline{\partial\mathcal{B}_{\boldsymbol{u}} \cup \partial\mathcal{B}_{\boldsymbol{t}}} = \overline{\partial\mathcal{B}_{p^{\mathrm{f}}} \cup \partial\mathcal{B}_{\boldsymbol{Q}_{\mathrm{f}}}} = \overline{\partial\mathcal{B}_\theta \cup \partial\mathcal{B}_{\boldsymbol{Q}_\theta}}, \tag{3.1}$$

$$\emptyset = \partial\mathcal{B}_{\boldsymbol{u}} \cap \partial\mathcal{B}_{\boldsymbol{t}} = \partial\mathcal{B}_{p^{\mathrm{f}}} \cap \partial\mathcal{B}_{\boldsymbol{Q}_{\mathrm{f}}} = \partial\mathcal{B}_\theta \cap \partial\mathcal{B}_{\boldsymbol{Q}_\theta}, \tag{3.2}$$

where $\partial\mathcal{B}_{\boldsymbol{u}}$ is the solid displacement boundary; $\partial\mathcal{B}_{\boldsymbol{t}}$ is the solid traction boundary; $\partial\mathcal{B}_p$ is the pore pressure boundary; $\partial\mathcal{B}_{\boldsymbol{Q}_{\mathrm{f}}}$ is the pore-fluid flux; $\partial\mathcal{B}_\theta$ is the temperature boundary; $\partial\mathcal{B}_{\boldsymbol{Q}_{\mathrm{f}}}$ is the heat flux boundary, as illustrated in Figure 3.

DOI: 10.1002/nme

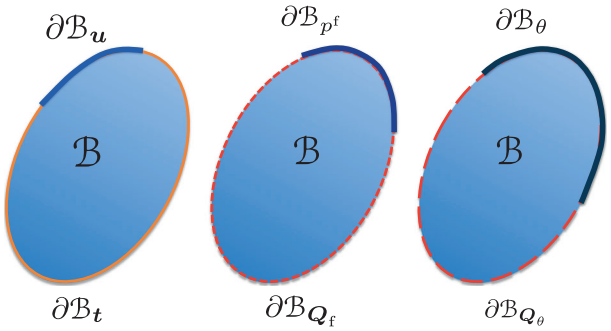

Figure 3. Domain and the corresponding boundaries of the thermo-hydro-mechanics problem. Figure reproduced from [53].

In summary, Dirichlet boundary conditions for the THM problem read

$$\begin{aligned} \boldsymbol{u} &= \overline{\boldsymbol{u}} \ \text{ on } \ \partial\mathcal{B}_{\boldsymbol{u}}, \\ p^{\mathrm{f}} &= \overline{p} \ \text{ on } \ \partial\mathcal{B}_{p}, \\ \theta &= \overline{\theta} \ \text{ on } \ \partial\mathcal{B}_{\theta}. \end{aligned} \tag{3.3}$$

Meanwhile, the von Neumann boundary conditions that describe the traction and fluxes read

$$\begin{aligned} \boldsymbol{N}\cdot\boldsymbol{P} &= \overline{\boldsymbol{t}} \ \text{ on } \ \partial\mathcal{B}_{\boldsymbol{t}}, \\ -\boldsymbol{N}\cdot\boldsymbol{Q}_{\mathrm{f}} &= \overline{Q}_{\mathrm{f}} \ \text{ on } \ \partial\mathcal{B}_{\boldsymbol{Q}_{\mathrm{f}}}, \\ -\boldsymbol{N}\cdot\boldsymbol{Q}_{\theta} &= \overline{Q}_{\theta} \ \text{ on } \ \partial\mathcal{B}_{\boldsymbol{Q}_{\theta}}. \end{aligned} \tag{3.4}$$

In addition, the spaces for the trial displacement, pore pressure, and temperature read

$$\begin{aligned} \boldsymbol{V}_{\boldsymbol{u}} &= \{\boldsymbol{u} : \mathcal{B} \to \mathbb{R}^3 | \boldsymbol{u} \in [H^1(\mathcal{B})]^3, \boldsymbol{u}|_{\partial\boldsymbol{B}_{\boldsymbol{u}}} = \overline{\boldsymbol{u}}\}, \\ V_p &= \{p^{\mathrm{f}} : \mathcal{B} \to \mathbb{R} | p^{\mathrm{f}} \in L^2(\mathcal{B}), p^{\mathrm{f}}|_{\partial\boldsymbol{B}_{p^{\mathrm{f}}}} = \overline{p^{\mathrm{f}}}\}, \\ V_{\theta} &= \{\theta : \mathcal{B} \to \mathbb{R} | \theta \in L^2(\mathcal{B}), \theta|_{\partial\boldsymbol{B}_{\theta}} = \overline{\theta}\}, \end{aligned} \tag{3.5}$$

where H^1 denotes the Sobolev space of degree one. The admissible variations of displacement $\boldsymbol{\eta}$, pore pressure ψ, and temperature θ therefore read

$$\begin{aligned} \boldsymbol{V}_{\boldsymbol{\eta}} &= \{\boldsymbol{\eta} : \mathcal{B} \to \mathbb{R}^3 | \boldsymbol{\eta} \in [H^1(\mathcal{B})]^3, \boldsymbol{\eta}|_{\partial\boldsymbol{B}_{\boldsymbol{\eta}}} = \boldsymbol{0}\}, \\ V_{\psi} &= \{\psi : \mathcal{B} \to \mathbb{R} | \psi \in L^2(\mathcal{B}), \psi|_{\partial\boldsymbol{B}_{p^{\mathrm{f}}}} = 0\}, \\ V_{\omega} &= \{\omega : \mathcal{B} \to \mathbb{R} | \psi \in L^2(\mathcal{B}), \omega|_{\partial\boldsymbol{B}_{\theta}} = 0\}. \end{aligned} \tag{3.6}$$

For brevity, the spatial argument $\boldsymbol{X} \in \mathcal{B}$ is not explicitly written. The weighted-residual statement of the balance of linear momentum, fluid content, and energy is as follows.

Find $\boldsymbol{u} \in \boldsymbol{V}_{\boldsymbol{u}}$, $p^{\mathrm{f}} \in V_{p^{\mathrm{f}}}$, and $\theta \in V_{\theta}$ such that for all $\boldsymbol{\eta} \in V_{\boldsymbol{\eta}}$ and $\psi \in V_{\psi}$ such that

$$G(\boldsymbol{u}, p^{\mathrm{f}}, \theta, \boldsymbol{\eta}) = H(\boldsymbol{u}, p^{\mathrm{f}}, \theta, \psi) = L(\boldsymbol{u}, p^{\mathrm{f}}, \theta, \omega) = 0, \tag{3.7}$$

where $G : \boldsymbol{V}_{\boldsymbol{u}} \times V_{p^{\mathrm{f}}} \times V_{\theta} \times V_{\eta} \to \mathbb{R}$ is the weak statement of the balance of linear momentum, that is,

$$\begin{aligned} G(\boldsymbol{u}, p^{\mathrm{f}}, \theta, \boldsymbol{\eta}) = &\int_{\mathcal{B}} \nabla^{\boldsymbol{X}}\cdot\boldsymbol{\eta} : \boldsymbol{P} - J(\rho^{\mathrm{f}} + \rho^{s})\boldsymbol{\eta}\cdot\boldsymbol{g} \ \mathrm{dV} \\ &- \int_{\partial\mathcal{B}_t} \boldsymbol{\eta}\cdot\overline{\boldsymbol{t}} \ \mathrm{d}\Gamma, \end{aligned} \tag{3.8}$$

DOI: 10.1002/nme

$H : \boldsymbol{V_u} \times V_{p^{\mathrm{f}}} \times V_\theta \times V_\psi \to \mathbb{R}$ is the weak statement of the balance of fluid content, that is,

$$\begin{aligned} H(\boldsymbol{u}, p^{\mathrm{f}}, \theta, \psi) = & \int_{\mathcal{B}} \psi \left(\frac{B}{J} - 3\alpha_s(\theta - \theta_o) \right) \dot{J} \ \mathrm{dV} \\ & + \int_{\mathcal{B}} \psi \frac{1}{M} \dot{p^f} - 3\psi\alpha^{\mathrm{m}}\dot{\theta} \ \mathrm{dV} \\ & - \int_{\mathcal{B}} \nabla^{\boldsymbol{X}} \psi \cdot \frac{1}{\rho_{\mathrm{f}}} \boldsymbol{W} \ \mathrm{dV} \\ & - \int_{\partial \boldsymbol{B}_Q} \psi \overline{Q}_{\mathrm{f}} \, \mathrm{d}\Gamma, \end{aligned} \tag{3.9}$$

and $L : \boldsymbol{V_u} \times V_{p^{\mathrm{f}}} \times V_\theta \times V_\omega \to \mathbb{R}$ is the weak statement of the balance of energy, that is,

$$\begin{aligned} L(\boldsymbol{u}, p^{\mathrm{f}}, \theta, \omega) = & \int_{\mathcal{B}} \omega \left(c_{\boldsymbol{F}} \dot{\theta} - 3\alpha_{\mathrm{sk}} K \theta \frac{\dot{J}}{J} - 3\alpha^{\mathrm{m}} \theta \dot{p^{\mathrm{f}}} \right) \ \mathrm{dV} \\ & + \int_{\mathcal{B}} \nabla^{\boldsymbol{X}} \omega \boldsymbol{k}_\theta \nabla^{\boldsymbol{X}} \dot{\theta} + \omega \frac{\Phi^f c_{\mathrm{f}}}{\rho_{\mathrm{f}}} \boldsymbol{W} \cdot \boldsymbol{F}^{-T} \cdot \nabla^{\boldsymbol{X}} \theta - \omega R_\theta \ \mathrm{dV} \\ & - \int_{\partial \boldsymbol{B}_Q} \omega \overline{Q}_\theta \ \mathrm{d}\Gamma. \end{aligned} \tag{3.10}$$

3.2. Temporal discretization

Because of the transient nature of the THM problem, the weak statement must be discretized in time. Typically, this temporal discretization is often conducted after the spatial discretization [54]. Here, we use a different approach in which temporal discretization will be considered before applying spatial discretization. This treatment is due to the usage of the template-based generic-programming-based package called Phalanx [55], which enables a component-based implementation and thus significantly simplify the programming efforts. This implementation method will be discussed in Section 4. As a result, we first derive an equivalent static problem [54] by discretizing the temporal domain before introducing basis functions for the spatial discretization. Here, we use finite difference approach in temporal domain such that the pore pressure and temperature at time step $n + 1$ can be written as

$$p^{\mathrm{f}}_{n+1} \approx p^{\mathrm{f}}_n + (1 - \hat{\beta})\Delta t \ \dot{p^{\mathrm{f}}}_n + \hat{\beta} \dot{p^{\mathrm{f}}}_{n+1}, \tag{3.11}$$

$$\theta_{n+1} \approx \theta_n + (1 - \hat{\beta})\Delta t \ \dot{\theta}_n + \hat{\beta}\dot{\theta}_{n+1}. \tag{3.12}$$

To simplify the formulation, we use the unconditionally stable fully backward Euler scheme by setting $\hat{\beta} = 1$. However, directly applying Euler scheme to discretize the Jacobian J in time will lead to erroneous results that make negative Jacobian possible. As a result, we take advantage of the following identity obtained via the chain rule:

$$\frac{D(\log J)}{Dt} = \frac{D \log J}{DJ} \frac{DJ}{Dt} = \frac{\dot{J}}{J}, \tag{3.13}$$

where $J \in \mathbb{R}^+$, $\log J \in \mathbb{R}$. Hence, we may obtain the material derivative of the Jacobian J by discretizing $\log J$ in time, that is,

$$J^{-1}_{n+1} \dot{J}_{n+1} = \frac{D}{Dt}(\log J_{n+1}) \approx \frac{\log J_{n+1} - \log J_n}{\Delta t}. \tag{3.14}$$

Substituting (3.11), (3.12), and (3.14) into weighted-residual form (3.7), the time discretized weighted-residual form reads

DOI: 10.1002/nme

$$\hat{G}\left(\boldsymbol{u}_{n+1}, p^{\mathrm{f}}_{n+1}, \theta_{n+1}, \boldsymbol{\eta}\right) = \hat{H}\left(\boldsymbol{u}_{n+1}, p^{\mathrm{f}}_{n+1}, \theta_{n+1}, \psi\right) = \hat{L}\left(\boldsymbol{u}_{n+1}, p^{\mathrm{f}}_{n+1}, \theta_{n+1}, \omega\right) = 0, \quad (3.15)$$

where the discrete weak form of the balance of linear momentum now reads

$$\begin{aligned}\hat{G}(\boldsymbol{u}_{n+1}, p^{\mathrm{f}}_{n+1}, \theta_{n+1}, \boldsymbol{\eta}) = &\int_{\mathcal{B}} \nabla^{\boldsymbol{X}} \cdot \boldsymbol{\eta} : \boldsymbol{P}_{\boldsymbol{n+1}} \, \mathrm{dV} \\ &- \int_{\mathcal{B}} J_{n+1}(\rho^{\mathrm{f}}_{n+1} + \rho^{\mathrm{s}}_{n+1}) \boldsymbol{\eta} \cdot \boldsymbol{g} \, \mathrm{dV} \\ &- \int_{\partial \mathcal{B}_t} \boldsymbol{\eta} \cdot \overline{\boldsymbol{t}}_{\boldsymbol{n+1}} \, \mathrm{d}\Gamma.\end{aligned} \quad (3.16)$$

Similarly, the discrete weak form of the balance of fluid content and balance of energy can be written as

$$\begin{aligned}\hat{H}(\boldsymbol{u}_{n+1}, p^{\mathrm{f}}_{n+1}, \theta_{n+1}, \psi) = &\int_{\mathcal{B}} \psi \left(B - 3\alpha_s(\theta_{n+1} - \theta_o) J_{n+1}\right) \frac{\log J_{n+1} - \log J_n}{\Delta t} \, \mathrm{dV} \\ &+ \int_{\mathcal{B}} \psi \left(\frac{1}{M_{n+1}} \frac{p^{\mathrm{f}}_{n+1} - p^{\mathrm{f}}_n}{\Delta t} - 3\alpha^{\mathrm{m}}_{n+1} \frac{\theta_{n+1} - \theta_n}{\Delta t} \right) \mathrm{dV} \\ &- \int_{\mathcal{B}} \nabla^{\boldsymbol{X}} \psi \cdot \frac{1}{\rho_{\mathrm{f}n+1}} \boldsymbol{W}_{n+1} \, \mathrm{dV} - \int_{\partial B_{\mathcal{Q}_{\mathrm{f}}}} \psi \overline{\boldsymbol{Q}}_{\mathrm{f}n+1} \, \mathrm{d}\Gamma.\end{aligned} \quad (3.17)$$

$$\begin{aligned}\hat{L}(\boldsymbol{u}_{n+1}, p^{\mathrm{f}}_{n+1}, \theta_{n+1}, \omega) = &\int_{\mathcal{B}} \omega \left(c_{\boldsymbol{F}n+1} \frac{\theta_{n+1} - \theta_n}{\Delta t} - 3K\alpha_{sk}\theta_{n+1} \frac{\log J_{n+1} - \log J_n}{\Delta t} \right) \mathrm{dV} \\ &- \int_{\mathcal{B}} \omega \left(3\alpha^{\mathrm{m}} \theta_{n+1} \frac{p^{\mathrm{f}}_{n+1} - p^{\mathrm{f}}_n}{\Delta t} + \frac{\Phi^{\mathrm{f}}_{n+1} c_{\mathrm{f}}}{\rho_{\mathrm{f}n+1}} \boldsymbol{W}_{n+1} \cdot \boldsymbol{F}^{-T}_{n+1} \cdot \nabla^{\boldsymbol{X}} \theta_{n+1} \right) \mathrm{dV} \\ &- \int_{\mathcal{B}} \nabla^{\boldsymbol{X}} \omega \cdot \boldsymbol{Q}_{\theta n+1} \, \mathrm{dV} - \int_{\partial B_{\mathcal{Q}_\theta}} \psi \overline{\boldsymbol{Q}}_{\theta n+1} \, \mathrm{d}\Gamma.\end{aligned} \quad (3.18)$$

Consider the case where the testing functions and the interpolated displacement, pore pressure, and temperature are spanned by the same basis functions. In that case, the following approximation holds:

$$\begin{aligned}\boldsymbol{u} \approx \boldsymbol{u}^h = \sum_{a=1}^{n} \boldsymbol{N}_a \boldsymbol{u}_a \;\; ; \;\; p^{\mathrm{f}} \approx p^{\mathrm{f}h} = \sum_{a=1}^{n} N_a p^{\mathrm{f}}_a \;\; ; \;\; \theta \approx \theta^h = \sum_{a=1}^{n} N_a \theta_a, \\ \boldsymbol{\eta} \approx \boldsymbol{\eta}^h = \sum_{a=1}^{n} \boldsymbol{N}_a \boldsymbol{\eta}_a \;\; ; \;\; \psi \approx \psi^h = \sum_{a=1}^{n} N_a \psi_a \;\; ; \;\; \omega \approx \omega^h = \sum_{a=1}^{n} N_a \omega_a,\end{aligned} \quad (3.19)$$

where $\boldsymbol{u}_a$, p^{f}_a, and θ_a are the nodal values of displacement, pore pressure, and temperature. $\boldsymbol{\eta}_a$, ψ_a, and ω_a are nodal values of the corresponding test functions. The resultant finite dimensional spaces for the interpolated displacement, pore pressure, and temperature are denoted as $\boldsymbol{V}^h_{\boldsymbol{u}}$, V^h_p, and V^h_θ, respectively. Similarly, we denote the finite dimensional space of the corresponding testing functions as $\boldsymbol{V}^h_{\boldsymbol{\eta}}$, V^h_ψ, and V^h_ω. The integer n is the number of node per element. By substituting (3.19) into (3.15), we obtain the equal-order Galerkin form of the thermo-hydro-mechanical problem.

3.3. Assumed deformation gradient for volumetric locking

In this section, we derive an assumed deformation gradient for the THM problem to circumvent the volumetric locking numerical deficiency. Recall that the kinematic split of the deformation gradient $\boldsymbol{F}$ is formulated as

$$\boldsymbol{F} = \boldsymbol{F}_{\mathrm{vol}} \cdot \boldsymbol{F}_{\mathrm{iso}}, \quad (3.20)$$

DOI: 10.1002/nme

where

$$\boldsymbol{F}_{\text{vol}} = J^{1/3}\boldsymbol{I} \;;\; \boldsymbol{F}_{\text{iso}} = J^{-1/3}\boldsymbol{F}. \tag{3.21}$$

Previously, the assumed deformation gradient method is often used to avoid the over-constraint associated with equal-order interpolations of the volumetric and isochoric parts of the deformation gradient [13, 56–59]. The key to avoid overconstraint is to replace the interpolated volumetric deformation field $J = \det \boldsymbol{F}$ with a reduced-order volumetric field $\overline{J}$ such that fewer volumetric constraints occur when incompressibility limit is approached. The resultant assumed deformation gradient is therefore composed of the modified volumetric deformation field and the original interpolated isochoric deformation gradient. In other words, the interpolated volumetric split $\boldsymbol{F}_{\text{vol}} = J^{1/3}\boldsymbol{I}$ is replaced by a modified definition $\overline{\boldsymbol{F}}_{\text{vol}} = \bar{J}^{1/3}\boldsymbol{I}$ such that

$$\overline{\boldsymbol{F}} = \bar{J}^{1/3}\boldsymbol{F}_{\text{iso}} = \bar{J}^{1/3}J^{-1/3}\boldsymbol{F}. \tag{3.22}$$

While the relaxation provided by the modification of deformation gradient definition is able to cure the locking issue, the usage of non-standard deformation gradient may lead to numerical instability as exhibited in [60, 61]. Moran *et al.* [56] suggested replacing the assumed deformation gradient $\overline{\boldsymbol{F}}$ with a linear interpolation between the original and the assumed deformation gradient, that is, $\widetilde{\boldsymbol{F}} = \alpha\boldsymbol{F} + (1-\alpha)\overline{\boldsymbol{F}}$, where α is a stabilization parameter in which $\alpha = 0$ leads to the pure F-bar formulation and $\alpha = 1$ leads to the standard formulation. The idea is to introduce stiffness to spurious zero-energy mode by increasing the magnitude of α whenever the numerical instability is encountered.

However, as deformation gradient belongs to multiplicative group, linear interpolation may lead to significant error. For instance, linearly interpolating rigid body rotations may lead to tensor not belonging to SO(3) group. To cure locking without comprising stability, we introduce a simple combined/standard F-bar element by recourse to exponential/logarithmic mapping for the THM problem in which the modified deformation gradient reads

$$\widetilde{\boldsymbol{F}} = \tilde{J}^{1/3}\boldsymbol{F}_{\text{iso}} = \tilde{J}^{1/3}J^{-1/3}\boldsymbol{F}, \tag{3.23}$$

where $\tilde{J}$ is the modified volumetric split of the deformation gradient, that is,

$$\tilde{J} = \exp\left(\frac{1-\beta}{\mathrm{V}_{\mathcal{B}^e}}\int_{\mathcal{B}^e}\log J \;\mathrm{dV} + \beta\log J\right), \tag{3.24}$$

where $\beta \in [0, 1]$ is a weighing parameter that partitions the standard and assumed deformation gradient. Augmented with the (2.17) and assumed that the thermal expansion coefficient α_{sk} is constant, the logarithmic volumetric strain $\log J$ reads

$$\log J = \log J^e + \log J^p + 3\alpha_{sk}(\theta - \theta_o). \tag{3.25}$$

The mechanical contribution of the assumed deformation gradient therefore reads

$$\widetilde{\boldsymbol{F}}_{\boldsymbol{M}} = \tilde{J}_{\boldsymbol{M}}^{1/3}\boldsymbol{F}_{\text{iso}}, \tag{3.26}$$

where

$$\tilde{J}_{\boldsymbol{M}} = \exp\left(\log\tilde{J} - 3\left(\frac{1-\beta}{\mathrm{V}_{\mathcal{B}^e}}\int_{\mathcal{B}^e}\alpha_{sk}\,(\theta-\theta_o)\;\mathrm{dV} + \beta\alpha_{sk}(\theta-\theta_o\;)\right)\right). \tag{3.27}$$

The combined formulation may reduce to the standard or F-bar formulation by adjusting α. Furthermore, it can be easily shown that (3.23) is identical to the mid-point assumed deformation gradient formulation in [58] if $\alpha = 0$, and the volume averaging of $\log J(X)$ is computed via one-point quadrature at the centroid of the element. In all the simulations presented in this paper, we found that setting $\alpha = 0.05$ appeared to eliminate the zero energy modes.

DOI: 10.1002/nme

Remark 2
At present, the optimal value of β is not known. While the assumed deformation gradient may lead to spurious modes for certain single-phase solid mechanics problems, non-zero β is not required in the solutions presented in the example section.

3.4. Inf-sup conditions and stabilization procedures

It is well known that isothermal hydro-mechanical responses near drained limit may maintain stability, even though displacement and pore pressure are interpolated by the same set of basis functions [21]. This seemingly stable responses nevertheless does not imply that the pore pressure and temperature will be free of spurious oscillations under different thermal and hydraulic conditions. In fact, when a very fine temporal discretization is used or when a simulation is conducted near the undrained limit, spurious pore pressure may occur because of the lack of inf-sup condition [13, 21, 22]. Similar spurious behaviors have also been observed in the THM problem. For instance, Liu *et al.* [53] study the onset of spurious temperature and pore pressure in small-strain non-isothermal hydro-mechanical finite element model and subsequently propose the usage of an interior penalty method to eliminate the oscillations in the pore pressure and temperature fields. The goal of this section is to develop a stabilized $\boldsymbol{u} - p^{\mathrm{f}} - \theta$ equal-order finite element THM problem, which eliminate spurious oscillation defined in (3.15).

We limit focus on our attention on a simplified model problem in which (1) the heat transfer and pore-fluid diffusion are both negligible, and (2) the skeleton deformation is only infinitesimal such that derivatives in material and current configurations are approximately the same.

Assumption (1) allows us to analyze the numerical stability of a porous medium at both the undrained and isentropic limits. Both undrained and isentropic conditions often constitute the worst-case scenario that is prone to spurious oscillations of pore pressure and temperature. Assumption (2) allows us to analyze the inf-sup condition raised in the linearized governing equation. This means that we will study the linear THM problem in the hope that this may give some indications on the more general nonlinear thermo-hydro-mechanical problem. A similar strategy has been adopted in Auricchio *et al.* [62], Pantuso and Bathe [63], and Auricchio *et al.* [64] to analyze the stability range of mixed finite element formulations for the large-strain incompressible elasticity problem. As pointed out previously by Pantuso and Bathe [63] and Auricchio *et al.* [64], schemes that are inf-sup stable in the linearized problem may still exhibit unphysical instabilities. Nevertheless, the inf-sup condition of the linear problem is still a valuable tool because it may serve as a necessary (but not sufficient) condition for maintaining numerical stability [63].

Here, we use the results from Howell and Walkington [65], who proves that finite element model with a saddle point structure form: $(\boldsymbol{u}^h, p^{\mathrm{f}h}, \theta^h) \in \boldsymbol{V_u}^h \times V_p^h \times V_\theta^h$, is well-posed if the finite dimensional spaces $\boldsymbol{V_u}^h$, V_p^h, and V_θ^h chosen for the displacement, pore pressure, and temperature interpolation satisfy the two-fold inf-sup condition, that is, there exists a constant $C_o > 0$ such that

$$\sup_{\boldsymbol{w}^h \in \boldsymbol{V_u}^h} \frac{\int_{\mathcal{B}} \left(p^{\mathrm{f}h} B + 3\theta K \alpha_{\mathrm{sk}}\right) \nabla^{\boldsymbol{x}} \boldsymbol{w}^h \, d\mathrm{V}}{||\boldsymbol{w}^h||_{\boldsymbol{V_u^h}}} \geqslant C_o \left(||p^{\mathrm{f}h}||_{V_p^h} + ||\theta^h||_{V_\theta^h}\right), \; (p^{\mathrm{f}h}, \theta^h) \in V_p^h \times V_\theta^h, \tag{3.28}$$

where $||\cdot||_{\boldsymbol{V_u^h}}$, $||\cdot||_{V_p^h}$, and $||\cdot||_{V_\theta^h}$ are the norms corresponding to the finite dimensional space $\boldsymbol{V}_u^h$, V_p^h, and V_θ^h. Here, we equip the spaces of the solutions and their corresponding testing functions with the same associated norms, that is,

$$\begin{aligned} ||\boldsymbol{u}||_{\boldsymbol{V_u}^h} &= ||\boldsymbol{u}||_1 = \sqrt{\int_{\mathcal{B}} \nabla^{\boldsymbol{x}} \boldsymbol{u} \cdot \nabla^{\boldsymbol{x}} \boldsymbol{u} \, dV}, \\ ||p||_{V_{p^{\mathrm{f}}}^h} &= \sqrt{\int_{\mathcal{B}} B p^2 \, dV}, \\ ||\theta||_{V_\theta^h} &= \sqrt{\int_{\mathcal{B}} 3\left(\alpha_{\mathrm{sk}} K\right) \theta^2 \, dV}. \end{aligned} \tag{3.29}$$

DOI: 10.1002/nme

Note that $||\cdot||_{V^h_{p^{\mathrm{f}}}}$, $||\cdot||_{V^h_\theta}$, and $||\cdot||_0$ are equivalent norms. Unfortunately, if displacement, pore pressure, and temperatures are all spanned by the same basis function, then the condition listed in (3.28) does not hold [66].

Our new contribution here is twofold. First, we prove that a weaker inf-sup bound also exists for the compound matrix $\mathbb{B}$. Then, for the first time, we propose a proper stabilization term that may eliminate the spurious oscillations of pore pressure and temperature for the THM problem.

3.4.1. Weak inf-sup conditions of coupling terms. To derive stabilized finite element formulation, we may first quantify the inf-sup 'deficiency' of the unstable, equal-order discretization, then propose additional terms to eliminate the spurious modes due to the inf-sup 'deficiency'. Previously, this strategy is used in Bochev *et al.* [25] where a weaker inf-sup bound is first identified for the Stokes equations, then a stabilization term is derived to restore stability for two interpolated velocity–pressure pairs.

To determine the weak inf-sup bound of individual coupling terms, let us first recall that the divergence is an isomorphism of the orthogonal complement of divergence-free functions in $\boldsymbol{H}^1_0(\mathcal{B})$ onto $L^2_0(\mathcal{B})$ space. Given that the pressure $p^{\mathrm{f}h} \in V^h_p \subset L^2_0(\mathcal{B})$, then the isomorphism of the divergence operator guarantees the existence of a $\boldsymbol{w} \in \boldsymbol{H}^1_0(\mathcal{B})$ such that

$$\nabla^{\boldsymbol{x}} \cdot \boldsymbol{w} = p^{\mathrm{f}h} \text{ and } ||\boldsymbol{w}||_1 \leqslant ||p^{\mathrm{f}h}||_{V^h_{p^{\mathrm{f}}}}. \tag{3.30}$$

With (3.30) in mind, we then have

$$\sup_{\boldsymbol{v}\in\boldsymbol{H}^1_o(\mathcal{B})} \frac{|\int_{\mathcal{B}} p^{\mathrm{f}h} B\nabla^{\boldsymbol{X}}\cdot\boldsymbol{v}\, d\mathrm{V}|}{||\boldsymbol{v}||_1} \geqslant \frac{\int_{\mathcal{B}} |\, p^{\mathrm{f}h} B\nabla^{\boldsymbol{X}}\cdot\boldsymbol{w}\, d\mathrm{V}|}{||\boldsymbol{w}||_1} \geqslant \frac{\int_{\mathcal{B}} |\, p^{\mathrm{f}h} B p^{\mathrm{f}h}\, d\mathrm{V}|}{||p^{\mathrm{f}h}||_{V^h_{p^{\mathrm{f}}}}} \geqslant \tilde{C}_p ||p^{\mathrm{f}h}||_{V^h_{p^{\mathrm{f}}}}, \tag{3.31}$$

where $\tilde{C}_p$ is a constant such that

$$\left|\int_{\mathcal{B}} p^{\mathrm{f}h} B\nabla^{\boldsymbol{x}}\cdot\boldsymbol{w}\, d\mathrm{V}\right| \geqslant \tilde{C}_p ||p^{\mathrm{f}h}||_{V^h_{p^{\mathrm{f}}}} ||\boldsymbol{w}||_1. \tag{3.32}$$

By letting $\boldsymbol{w}^h$ be the interpolant of $\boldsymbol{v}$ of $\boldsymbol{V^u}$ and using the well-known approximation result of [67, p. 217], that is, $||\boldsymbol{w}-\boldsymbol{w}^h||_{V^h_{p^{\mathrm{f}}}} \leqslant Ch||\boldsymbol{w}||_1$; $||\boldsymbol{w}^h||_1 \leqslant C||\boldsymbol{w}||_1$ and the fact that $||\cdot||_0$ and $||\cdot||_{V^h_{p^{\mathrm{f}}}}$ are equivalent norms, we obtain

$$\begin{aligned}
\sup_{\boldsymbol{v}^h\in\boldsymbol{V^h_u},\boldsymbol{v}\neq\boldsymbol{0}} \frac{\int_{\mathcal{B}} p^{\mathrm{f}h} B\nabla^{\boldsymbol{x}}\cdot\boldsymbol{v}^h\, d\mathrm{V}}{||\boldsymbol{v}^h||_1} &\geqslant \frac{|\int_{\mathcal{B}} p^{\mathrm{f}h} B\nabla^{\boldsymbol{x}}\cdot\boldsymbol{w}^h\, d\mathrm{V}|}{||\boldsymbol{w}||_1} \\
&\geqslant \frac{\int_{|\mathcal{B}} p^{\mathrm{f}h} B\nabla^{\boldsymbol{x}}\cdot\boldsymbol{w}\, d\mathrm{V}|}{||\boldsymbol{w}||_1} - \frac{|\int_{\mathcal{B}} p^{\mathrm{f}h} B\nabla^{\boldsymbol{x}}\cdot(\boldsymbol{w}-\boldsymbol{w}^h)\, d\mathrm{V}|}{||\boldsymbol{w}||_1} \\
&\geqslant \frac{\tilde{C}_p}{C}||p^{\mathrm{f}h}||_{V^h_{p^{\mathrm{f}}}} - \frac{||\nabla^{\boldsymbol{x}} p^{\mathrm{f}h}||_{V^h_{p^{\mathrm{f}}}} ||\boldsymbol{w}^h-\boldsymbol{w}||_{V^h_{p^{\mathrm{f}}}}}{C||\boldsymbol{w}||_{V^h_{p^{\mathrm{f}}}}}.
\end{aligned} \tag{3.33}$$

Therefore,

$$\sup_{\boldsymbol{v}^h\in\boldsymbol{V^h_u},\boldsymbol{v}\neq\boldsymbol{0}} \frac{\int_{\mathcal{B}} p^{\mathrm{f}h} B\nabla^{\boldsymbol{x}}\cdot\boldsymbol{v}^h\, d\mathrm{V}}{||\boldsymbol{v}^h||_1} \geqslant \alpha_1 ||p^{\mathrm{f}h}||_{V^h_{p^{\mathrm{f}}}} - \alpha_2 h||\nabla^{\boldsymbol{x}} p^{\mathrm{f}h}||_{V^h_{p^{\mathrm{f}}}},\ p^{\mathrm{f}h} \in V^h_p, \tag{3.34}$$

where h is the mesh size, and C, α_1, and α_2 are constants. Following the same logic, it is trivial to show that the same procedure can be applied to the thermo-elastic coupling term, that is,

DOI: 10.1002/nme

$$\sup_{\boldsymbol{w}^h \in \boldsymbol{V}_{\boldsymbol{u}}^{\boldsymbol{h}}, \boldsymbol{v} \neq \boldsymbol{0}} \frac{\int_{\mathcal{B}} 3K\alpha_{\mathrm{sk}} \theta^h \nabla^{\boldsymbol{x}} \cdot \boldsymbol{w}^h \, d\mathrm{V}}{||\boldsymbol{w}^h||_1} \geqslant \beta_1 ||\theta^h||_{V_{\theta^h}} - \beta_2 h ||\nabla^{\boldsymbol{x}} \theta^h||_{V_{\theta^h}} \, , \theta^h \in V_\theta^h, \tag{3.35}$$

where β_1 and β_2 are positive constant.

3.4.2. Combined weak inf-sup condition. Our goal here is to use the weak inf-sup bounds of individual coupling terms expressed in (3.34) and (3.35) to define a weak inf-sup bound for the THM problem.

First, note that (3.34) can be written as

$$\begin{aligned} \sup_{\boldsymbol{v}^h \in \boldsymbol{V}_{\boldsymbol{u}}^{\boldsymbol{h}}, \boldsymbol{v} \neq \boldsymbol{0}} \frac{\int_{\mathcal{B}} p^{\mathrm{f}h} B \nabla^{\boldsymbol{x}} \cdot \boldsymbol{v}^h \, d\mathrm{V}}{||\boldsymbol{v}^h||_1} &= \sup_{\boldsymbol{v}^h \in \boldsymbol{V}_{\boldsymbol{u}}^{\boldsymbol{h}}, \boldsymbol{v} \neq \boldsymbol{0}} \int_{\mathcal{B}} p^{\mathrm{f}h} B \nabla^{\boldsymbol{x}} \cdot \left(\frac{\boldsymbol{v}^h}{||\boldsymbol{v}^h||_1} \right) d\mathrm{V} \\ &= \sup_{\boldsymbol{v}^h \in \boldsymbol{V}_{\boldsymbol{u}}^{\boldsymbol{h}}, ||\boldsymbol{v}^h||_1 = 1} \int_{\mathcal{B}} p^{\mathrm{f}h} B \nabla^{\boldsymbol{x}} \cdot \boldsymbol{v}^h \, d\mathrm{V}. \end{aligned} \tag{3.36}$$

As a result, (3.34) can be rewritten as

$$\sup_{\boldsymbol{v}^h \in \boldsymbol{V}_{\boldsymbol{u}}^{\boldsymbol{h}}, ||\boldsymbol{v}^h||_1 = 1} \int_{\mathcal{B}} p^{\mathrm{f}h} B \nabla^{\boldsymbol{x}} \cdot \boldsymbol{v}^h \, d\mathrm{V} \geqslant \alpha_1 ||p^{\mathrm{f}h}||_{V_{p^{\mathrm{f}}}^h} - \alpha_2 h ||\nabla^{\boldsymbol{x}} p^{\mathrm{f}h}||_{V_{p^{\mathrm{f}}}^h}. \tag{3.37}$$

Applying the same argument on (3.35), we have

$$\sup_{\boldsymbol{w}^h \in \boldsymbol{V}_{\boldsymbol{u}}^{\boldsymbol{h}}, ||\boldsymbol{v}^h||_1 = 1} \int_{\mathcal{B}} 3K\alpha_{\mathrm{sk}} \theta^h \nabla^{\boldsymbol{x}} \cdot \boldsymbol{w}^h \, d\mathrm{V} \geqslant \beta_1 ||\theta^h||_{V_{\theta^h}} - \beta_2 h ||\nabla^{\boldsymbol{x}} \theta^h||_{V_{\theta^h}}. \tag{3.38}$$

Note that (3.37) implies the existence of $\boldsymbol{v}^h \in \boldsymbol{V}_{\boldsymbol{u}^h}$ with $||\boldsymbol{v}^h||_1 = 1$ such that

$$\int_{\mathcal{B}} p^{\mathrm{f}h} B \nabla^{\boldsymbol{x}} \cdot \boldsymbol{v}^h \, d\mathrm{V} \geqslant C_1 ||p^{\mathrm{f}h}||_{V_{p^{\mathrm{f}}}^h} - C_2 h ||\nabla^{\boldsymbol{x}} p^{\mathrm{f}h}||_{V_{p^{\mathrm{f}}}^h}, p^{\mathrm{f}h} \in V_p^h. \tag{3.39}$$

On the other hand, (3.38) implies the existence of $\boldsymbol{w}^h \in \boldsymbol{V}_{\boldsymbol{w}^h}$ with $||\boldsymbol{w}^h||_1 = 1$ such that

$$\int_{\mathcal{B}} 3K\alpha_{\mathrm{sk}} \theta^h \nabla^{\boldsymbol{x}} \cdot \boldsymbol{w}^h \, d\mathrm{V} \geqslant \beta_1 ||\theta^h||_{V_\theta^h} - \beta_2 h ||\nabla^{\boldsymbol{x}} \theta^h||_{V_\theta^h} \, , \theta^h \in V_\theta^h. \tag{3.40}$$

Now, let $\boldsymbol{u} = \boldsymbol{v}^h + \boldsymbol{w}^h$, then

$$\begin{aligned} \int_{\mathcal{B}} p^{\mathrm{f}h} B \nabla^{\boldsymbol{x}} \cdot \boldsymbol{u} \, d\mathrm{V} &= \int_{\mathcal{B}} p^{\mathrm{f}h} B \nabla^{\boldsymbol{x}} \cdot \boldsymbol{v}^h \, d\mathrm{V} + \int_{\mathcal{B}} p^{\mathrm{f}h} B \nabla^{\boldsymbol{x}} \cdot \boldsymbol{w}^h \, d\mathrm{V} \\ &= \int_{\mathcal{B}} p^{\mathrm{f}h} B \nabla^{\boldsymbol{x}} \cdot \boldsymbol{v}^h \, d\mathrm{V} + \int_{\mathcal{B}} \frac{B p^{\mathrm{f}h}}{3K\alpha_{\mathrm{sk}}} (3K\alpha_{\mathrm{sk}}) \nabla^{\boldsymbol{x}} \cdot \boldsymbol{w}^h \, d\mathrm{V}, \\ \int_{\mathcal{B}} 3K\alpha_{\mathrm{sk}} \theta^h \nabla^{\boldsymbol{x}} \cdot \boldsymbol{u} \, d\mathrm{V} &= \int_{\mathcal{B}} 3K\alpha_{\mathrm{sk}} \theta^h \nabla^{\boldsymbol{x}} \cdot \boldsymbol{v}^h \, d\mathrm{V} + \int_{\mathcal{B}} 3K\alpha_{\mathrm{sk}} \theta^h \nabla^{\boldsymbol{x}} \cdot \boldsymbol{v}^{\boldsymbol{w}} \, d\mathrm{V} \\ &= \int_{\mathcal{B}} \frac{3K\alpha_{\mathrm{sk}} \theta^h}{B} B \nabla^{\boldsymbol{x}} \cdot \boldsymbol{v}^h \, d\mathrm{V} \int_{\mathcal{B}} 3K\alpha_{\mathrm{sk}} \theta^h \nabla^{\boldsymbol{x}} \cdot \boldsymbol{w}^h \, d\mathrm{V}. \end{aligned} \tag{3.41}$$

Recall that $V_{p^{\mathrm{f}}}^h$ and V_θ^h are spanned by the same set of basis functions. Thus, $\tilde{p}^h = (3K\alpha_{\mathrm{sk}}/B)\theta^h$ and $\tilde{\theta}^h = (B/(3K\alpha_{\mathrm{sk}}))\, p^{\mathrm{f}h}$, we have

DOI: 10.1002/nme

$$\int_{\mathcal{B}} \left(p^{\mathrm{f}h} B + 3K\alpha_{\mathrm{sk}}\theta^h\right) \nabla^{\boldsymbol{x}} \cdot \boldsymbol{u}\, d\mathrm{V} = \int_{\mathcal{B}} \left(p^{\mathrm{f}h} + \tilde{p}^h\right) B \nabla^{\boldsymbol{x}} \cdot \boldsymbol{v}^h\, d\mathrm{V} + \int_{\mathcal{B}} 3K\alpha_{\mathrm{sk}} \left(\theta^h + \tilde{\theta}^h\right) \nabla^{\boldsymbol{x}} \cdot \boldsymbol{w}^h\, d\mathrm{V} \geqslant \gamma_1 \left(||p^{\mathrm{f}h}||_{V^h_{p^{\mathrm{f}}}} + ||\theta^h||_{V^h_\theta}\right) - \gamma_2 h \left(||\nabla^{\boldsymbol{x}} p^{\mathrm{f}h}||_{V^h_{p^{\mathrm{f}}}} + ||\nabla^{\boldsymbol{x}} \theta^h||_{V^h_\theta}\right), \tag{3.42}$$

where $\gamma_1 = \min(\alpha_1, \beta_1)$, and $\gamma_2 = \max(\alpha_2, \beta_2)$. Thus, according to the definition of supremum, we may express the combined weaker inf-sup bound as

$$\sup_{\boldsymbol{v}^h \in \boldsymbol{V}^h_{\boldsymbol{u}}, \boldsymbol{v} \neq \boldsymbol{0}} \frac{\int_{\mathcal{B}} \left(p^{\mathrm{f}h} B + 3K\alpha_{\mathrm{sk}}\theta^h\right) \nabla^{\boldsymbol{x}} \cdot \boldsymbol{v}^h\, d\mathrm{V}}{||\boldsymbol{v}^h||_1} \geqslant C_1 \left(||p^{\mathrm{f}h}||_{V^h_{p^{\mathrm{f}}}} + ||\theta^h||_{V^h_\theta}\right) - C_2 h \left(||\nabla^{\boldsymbol{x}} p^{\mathrm{f}h}||_{V^h_{p^{\mathrm{f}}}} + ||\nabla^{\boldsymbol{x}} \theta^h||_{V^h_\theta}\right), \tag{3.43}$$

where C_1 and C_2 are positive constant.

3.4.3. Projection-based stabilization. By comparing (3.28) and (3.43), we notice that the difference between the inf-sup bound and the weak inf-sup bound is the gradient term in (3.43), that is,

$$- C_2 h \left(||\nabla^{\boldsymbol{x}} p^{\mathrm{f}h}||_{V^h_{p^{\mathrm{f}}}} + ||\nabla^{\boldsymbol{x}} \theta^h||_{V^h_\theta}\right). \tag{3.44}$$

This term can be used as a template for the design of stabilization terms. For instance, a simple remedy to restore numerical stability by directly adding perturbation gradient terms in (3.43) such that the inf-sup deficiency is counterbalanced. Here, we consider an alternative characterization of the inf-sup deficiency formulated in terms of projection operators. The upshot of a projection-based stabilization method is that it does not depend on the mesh size h or the type of element shapes, hence, easier to be implemented. As discussed in Sun *et al.* [13], the rationale of the projection-based stabilization is based on the inverse inequality, which guarantees the existence of a positive constant C_I such that

$$C_I h \left(||\nabla^{\boldsymbol{x}} p^{\mathrm{f}h}||_{V^h_{p^{\mathrm{f}}}} + ||\nabla^{\boldsymbol{x}} \theta^h||_{V^h_\theta}\right) \leqslant ||p^{\mathrm{f}h} - \Pi p^{\mathrm{f}h}||_{V^h_{p^{\mathrm{f}}}} + ||\theta^h - \Pi\theta^h||_{V^h_\theta}, \tag{3.45}$$

where $\Pi(\cdot)$ is a projection operator leads to a piecewise constant field. Here, we define $\Pi(\cdot)$ as simply the element average operator that reads

$$\Pi(\cdot) = \frac{1}{V^e} \int_K (\cdot)\, d\mathrm{V}\ ; K \in \mathcal{B}. \tag{3.46}$$

Furthermore, because it is not clear whether the two-way couplings between pore-fluid diffusion and heat transfer may destabilize the system if either the pore-fluid or the thermal conductivity is too low, we introduce a third term as a safety measure. The resultant perturbation functional reads

$$W^{per}(\theta^h, p^{\mathrm{f}h}) = C \left(\frac{1}{2}||p^{\mathrm{f}h} - \Pi p^{\mathrm{f}h}||^2_{V^h_{p^{\mathrm{f}}}} + \frac{1}{2}||\theta^h - \Pi\theta^h||^2_{V^h_\theta} + \sum_{K \in \Omega} \left| \int_K 3\alpha^m (p^{\mathrm{f}h} - \Pi p^{\mathrm{f}h})(\theta^h - \Pi\theta^h) d\mathrm{V} \right|\right), \tag{3.47}$$

DOI: 10.1002/nme

where C is a positive constant. The stabilization term added to the discrete balance of mass Equation (3.17) is simply the first variation of (3.47) with respect to pore pressure, that is,

$$\begin{aligned}\hat{H}^{\text{stab}}(\psi, p^{\text{f}h}_{n+1}, \theta^h_{n+1}) = &\sum_{K\in\mathcal{B}}\int_K C_{p1}(\psi - \Pi\psi)\left(p^{\text{f}h}_{n+1} - p^{\text{f}h}_n - \Pi\left(p^{\text{f}h}_{n+1} - p^{\text{f}h}_n\right)\right)d\text{V}\\ &+ \sum_{K\in\mathcal{B}}\int_K C_{p2}(\psi - \Pi\psi)\left(\theta^h_{n+1} - \theta^h_n - \Pi\left(\theta^h_{n+1} - \theta^h_n\right)\right)d\text{V}.\end{aligned} \tag{3.48}$$

On the other hand, the stabilization term added to the balance of energy (3.17) is obtained by taking the first variation of (3.47) with respect to temperature and multiply the result by the temperature, that is,

$$\begin{aligned}\hat{L}^{\text{stab}}(\omega, p^{\text{f}h}_{n+1}, \theta^h_{n+1}) = &\sum_{K\in\mathcal{B}}\int_K C_{\theta1}(\omega - \Pi\omega)\theta^h_{n+1}\left(p^{\text{f}h}_{n+1} - p^{\text{f}h}_n - \Pi\left(p^{\text{f}h}_{n+1} - p^{\text{f}h}_n\right)\right)d\text{V}\\ &+ \sum_{K\in\mathcal{B}}\int_K C_{\theta2}(\omega - \Pi\omega)\left(\theta^h_{n+1} - \theta^h_n - \Pi\left(\theta^h_{n+1} - \theta^h_n\right)\right)d\text{V},\end{aligned} \tag{3.49}$$

where C_{p1}, C_{p2}, $C_{\theta1}$, and $C_{\theta2}$ are the stabilization parameters. Finally, applying the stabilized formulation in the discrete variational Equation (3.15) yields

$$\begin{aligned}\hat{G}\left(\boldsymbol{u}^h_{n+1}, p^{\text{f}h}_{n+1}, \theta^h_{n+1}, \boldsymbol{\eta}\right) &= 0,\\ \hat{H}\left(\boldsymbol{u}^h_{n+1}, p^{\text{f}h}_{n+1}, \theta^h_{n+1}, \psi\right) - \hat{H}^{\text{stab}}\left(\boldsymbol{u}^h_{n+1}, p^{\text{f}h}_{n+1}, \theta^h_{n+1}, \psi\right) &= 0,\\ \hat{L}\left(\boldsymbol{u}^h_{n+1}, p^{\text{f}h}_{n+1}, \theta^h_{n+1}, \omega\right) - \hat{L}^{\text{stab}}\left(\boldsymbol{u}^h_{n+1}, p^{\text{f}h}_{n+1}, \theta^h_{n+1}, \omega\right) &= 0.\end{aligned} \tag{3.50}$$

While stabilization procedure provides a convenient and simple way to eliminate spatial oscillations from equal-order mixed finite element, the selection of stabilization parameter(s) remains a challenging problem [68]. This problem is further complicated by the fact that the heat transfer and pore-fluid diffusion may occur at different spatial and time scales and therefore making it difficult to select a stabilization parameter that ensures both spatial stability but avoid over-diffusion for both processes.

Our objective here is to provide a rough estimation of the optimal value of stabilization parameters. These estimated parameters can be served as useful guidelines for tuning the stabilization parameters, but they should not be viewed as the definitive choices for a given THM problem. The influence of the stabilization parameter will be further tested via numerical experiments presented in Section 5. Here, we recommend the following stabilization parameters for Equation (3.50):

$$\begin{aligned}C_{p1} &= \alpha\left[\frac{2G(1-\nu)}{1-2\nu}\left(\frac{B^2(1+\nu_u)^2(1-2\nu)}{9(1-\nu_u)(\nu_u-\nu)}\right)\right]^{-1},\\ C_{p2} &= \alpha\frac{2(\nu_u-\nu)}{B(1+\nu_u)(1-\nu)}\left[\alpha_{\text{sk}} + \frac{B(1-\nu)(1+\nu_u)}{2(\nu_u-\nu)}\alpha_m\right],\\ C_{\theta1} &= \alpha\left[c_{\boldsymbol{F}} + \frac{9\theta\alpha^2_{\text{sk}}K^2}{K+4G/3}\right],\\ C_{\theta2} &= \alpha\left[\frac{3\alpha_{sk}K}{K+4/3G} - 3\alpha_m\right]\theta,\end{aligned} \tag{3.51}$$

where α is the safety factor. ν_u is the undrained void ratio, which reads

$$\nu_u = \frac{3\nu + B(1-2\nu)(1-K/K_s)}{3 - B(1-2\nu)(1-K/K_s)}. \tag{3.52}$$

DOI: 10.1002/nme

The stabilization parameters are inferred from the simplified linear thermo-hydro-mechanical problem in Coussy [1, p.136]. In particular, we use the previous results from Preisig and Prévost [6] and Sun *et al.* [13], who show that by setting parameter $\alpha = 1$, one may recover the stable lumped mass formulation for one-dimensional problems.

4. HIGHLIGHTS OF THE IMPLEMENTATION METHOD

The THM model described in the previous sections is implemented in an open source, component-based finite element code called Albany [69–71]. Broadly speaking, the Albany code acts as a 'glue code' that integrates multiple re-usable libraries. Many of these libraries are available in the Trilinos project [72]. The key feature of Albany is the template-based programming approach, which allows developers to implement the finite element residuals by decomposing them into expression objects. These expression objects can be physical quantities (e.g., permeability, thermal conductivity, and deformation) or mathematical entities, such as sets, points, lines, graphs, functions, and boundary conditions.

The Albany code also features a graph-based software design, which has been employed previously in Notz *et al.* [73] to model thermo-fluid problem and in Sun *et al.* [13] to model isothermal hydro-mechanical responses of porous media. This section is intended to provide a brief account about the implementation of the THM problem via this new technique developed by Salinger *et al.* [71]. Readers interested at the software design and details of the Albany code, please refer to Notz *et al.* [73], Pawlowski *et al.* [69] and Salinger *et al.* [71] for further details.

Our starting point is the stabilized Galerkin form listed in (3.50) where the standard Gaussian integration is used to compute the integrands. To assembly the balance laws listed in (3.50), we decompose the discretized PDE systems into a directed graph, a mathematical object formed by a collection of vertices and directed edges. In our case, the vertices are the expressions that form the discretized PDE system, and the directed edges indicate the data hierarchical dependence. The decomposition of residuals are done while following the rules listed subsequently.

- The residual equations are always at the top of the hierarchy, that is, the source vertices in the directed graph.
- The nodal solutions are always at the bottom of the hierarchy, that is, the sink vertices of the directed graph.
- The directed graph formed by the decomposed expression objects must be acyclic, which means that there must be no cycle in the directed graph.

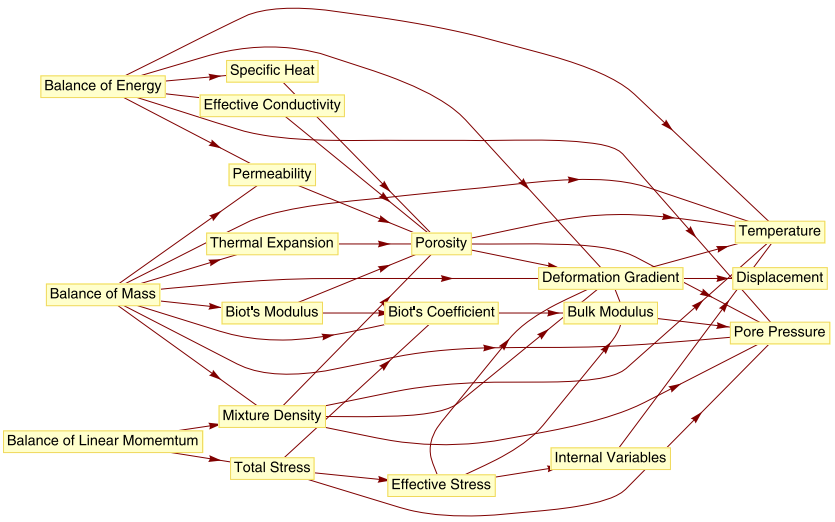

Figure 4. Directed graph that represents the hierarchy of mathematical expressions for thermo-hydro-mechanical problems.

DOI: 10.1002/nme

– All expressions in the directed graph must be connected, that is, no isolated vertex in the directed graph.

Figure 4 shows a directed graph used to assemble the residuals of the thermo-hydro-mechanical model. One salient feature of this implementation approach is the transparency of data dependence. Even for multi-physical processes with very complicated coupling mechanisms, such as the THM problem, one may still explore, examine, and modify the topology of mathematical models in a visual way.

In the thermo-hydro-mechanical model, each expression in the vertex is implemented as an evaluator [69, 70]. An evaluator stores numerical values of the expression (e.g., permeability, thermal conductivity, and equivalent plastic strain at the quadrature points of each finite element), record the location of the expression in the directed graph, and contains the actual code that compute the numerical values of the expressions (e.g., Equations 2.9, (2.39), (3.24), and 2.26). Residual vectors and the consistent tangent stiffness matrix are then computed via automatic differentiation performed on the directed graph via the Phalanx package [69, 70]. As a result, there is no need to derive the linearized forms of the variational equations.

5. NUMERICAL EXAMPLES

We present a selection of numerical examples to validate the implementation of the finite element model and demonstrate the three-way coupling effects of thermo-sensitive porous media at geometrically nonlinear regime. In particular, we will use the first example to address the numerical stability issue associated with material near undrained and adiabatic limits. The mechanical response of the solid skeleton is assumed to be elastic and replicated by a rate-independent neo-Hookean model. Because of the three-way coupling effects, the pore pressure evolves in a non-monotonic manner. This non-monotonic change is due to the Mandel–Cryer effect. Previously, the Mandel–Cryer effect has been observed in small-strain numerical simulations of drained sphere [45]. Here, our new contribution is to demonstrate the Mandel–Cryer effect of the undrained sphere at finite strain.

In the second example, we will examine the formation of shear band in a globally undrained specimen. The specimen is not in an isothermal condition. Thus, solid response is affected by the thermal expansion of both the solid and fluid constituents. The heat transfer is governed by a coupled diffusion–convection equation in which temperature changes at a material point can be caused by the structural heating, plastic dissipation, as well as the heat and pore-fluid fluxes. In both examples, we assume that there is no phase transition occurred.

5.1. Heated globally undrained porous sphere

In this numerical example, we simulate an undrained porous sphere heated by a raised temperature prescribed at the outer boundary. The purpose of this example is to demonstrate the performance of the stabilization scheme when thermal and pore-fluid diffusion occur at different time scales. The outer boundary of the sphere is subjected to a zero-Darcy-velocity boundary condition, and thus the sphere is globally undrained. The temperature of the surface of the sphere is prescribed, while the rest of the sphere is initially at zero degree. Because of the rotational symmetry, only $1/8$ of the spherical domain is meshed. The radius of the sphere is 1 m. The material parameters used to conduct these simulations are listed in Table I. To illustrate how the stabilization term may alter the numerical solution, we conduct three numerical simulations with different stabilization parameters ($\alpha = 0, 1, 8$). It should be noted that the globally undrained porous sphere problem presented here might not be the worst case scenario for spatial stability. For instance, other benchmark problems, such as the generalized Terzaghi's one-dimensional consolidation problem coupled with heat transfer and the heated porous spherical problem with a fully permeable boundary, are also known to generate sharp pressure gradients and spurious oscillations at early time. For brevity, these problems are not included in this paper, but will be explored in future study. In this example, a combination of low permeability and small time step is used to trigger the spurious oscillation in this numerical examples. This method has been used in Preisig and Prévost [6] and Sun *et al.* [13] to trigger spurious oscillation for isothermal poromechanics problem. The theoretical basis for the onset of spurious

DOI: 10.1002/nme

Table I. Material properties of the undrained sphere in non-isothermal condition.

Parameter	Description	Value	Unit
E	Young's modulus	2000	MPa
ν	Poisson's ratio	0.10	Dimensionless
T_o	Reference temperature	0	°C
α_s	Skeleton thermal expansion	8.3×10^{-5}	1/°C
α_f	Pore-fluid thermal expansion	6.9×10^{-5}	1/°C
ρ_s	Solid constituent density	2700	kg/m^3
ρ_f	Fluid constituent density	1000	kg/m^3
c_s	Solid specific heat	1700	J/kg/°C
c_f	Fluid specific heat	4200	J/kg/°C
k^s_θ	Solid thermal conductivity	2.50	W/m/°C
k^f_θ	Fluid thermal conductivity	2.50	W/m/°C
K_s	Solid grain bulk modulus	50	GPa
K_f	Fluid bulk modulus	20	GPa
k_o	Kozeny–Carmen coefficient	1×10^{-19}	m/s
μ	Viscosity	1.0×10^{-3}	Pa·s
ϕ^f	Initial porosity	0.25	Dimensionless

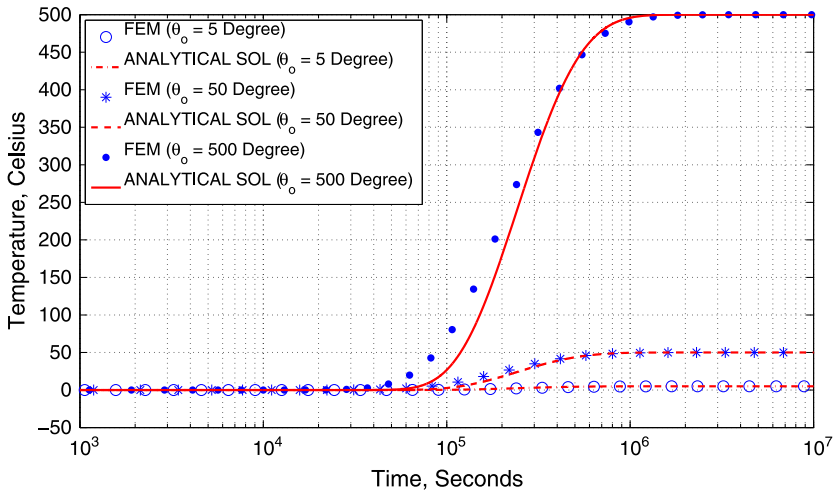

Figure 5. Comparison of the finite element solution and the analytical solution for three cases where $\theta_o = 5, 50,$ and 500°C.

oscillation can be found in the one-dimensional analyses by Harari [74], Preisig and Prévost [6], and Sun *et al.* [13].

5.1.1. Verification of a limiting case. Figure 5 shows the simulated and analytical transient thermal responses of center when the prescribed temperature $\theta_o = 5, 50,$ and 500°C. The analytical solution is obtained by neglecting the poro-elasticity coupling effect. Using Laplace transform [45], the temperature at the center is

$$\theta(t) = \theta_o - 2\theta_o \left[\sum_{n=1}^{\infty} (-1)^{n+1} \exp\left(-n^2\pi^2\tau\right) \right] \; ; \; \tau = \frac{K_\theta t}{R_o^2 \left((1-\phi^f)\rho_\theta^s c_s + \phi^f \rho_\theta^f c_f \right)}, \quad (5.1)$$

where $R_0 = 1m$ is the radius of the sphere, and θ_o is the temperature prescribed at the surface. Previously, Selvadurai and Suvorov [45] observed that for certain limited case where (1) fluid and solid constituents are incompressible, and (2) thermal convection and structural heating are not important, thermal diffusion of a spherical object can be solved via Laplace transform in a decoupled manner. In this example, we purposely use nearly incompressible constituents and make the solid skeleton

DOI: 10.1002/nme

nearly impermeable to compare analytical and finite element solutions. According to Figure 5, the temperature obtained from the finite strain THM simulation is very similar to the analytical solution obtained via (5.1) when $\theta_o = 5°C$. This is attributed to the fact the permeability is relatively low, and the material is stiff. The temperature changes because of structural heating and convection due to fluid transport are therefore very limited, when the prescribed temperature is close to the initial body temperature. Nevertheless, as we increase the prescribed temperature while holding the initial body temperature constant, the discrepancy between the coupled and decoupled simulations does become more significant, as shown in Figure 5, where $\theta_o = 50$ and $\theta_o = 500°C$.

Remark 3
The code has also been verified via a number of analytical solutions under the isothermal condition in Sun *et al.* [13]. For brevity, the verification problems for the isothermal case are not included in this article. Interested readers please refer to Sun *et al.* [13] for details.

5.1.2. Assessments of the stabilization procedure. Figure 6 shows the pore pressure of the undrained sphere 1 second after it was put into the 5° heat bath. Figure 6(a) is obtained from the stabilized FEM simulation, while Figure 6(b) is obtained without any stabilization procedure. Because of the low permeability, spatial oscillations of pore pressure occur in the standard equal-order THM element, while the stabilized equal-order THM element is able to deliver smooth pore pressure. On the other hand, Figure 7 compares the temperature at time= 1 s from the stabilized and standard FEM simulations. Because the thermal conductivity is relatively high, one may expect that the temperature would not exhibit any spatial oscillation even with standard FEM simulations. Yet, the simulation results show that the coupling between pore-fluid diffusion and heat transfer alone is significant enough to trigger spatial oscillation in the temperature field. This example demonstrates that the spurious oscillation of the temperature field can be triggered by an unstable pore pressure field, even when the thermal diffusivity is high. On the other hand, results demonstrated in Figures 6 and 7 indicate that the stabilization procedure is able to eliminate the spurious oscillations in both pore pressure and temperature. As reported in Sun *et al.* [13], Tezduyar and Osawa [68], White and Borja [21], stabilization procedures may eliminate spurious oscillations, but it may also over-diffuse the numerical solutions and lead to incorrect conclusion. To determine whether the stabilization procedure proposed in Section 3.4.3 is able to eliminate spurious modes without over-diffusing the solutions, we conduct two numerical simulations on the undrained sphere, one with stabilization (i.e., $\alpha = 1$), and a control test without stabilization (i.e., $\alpha = 0$).

Figure 8 compares the temperature and pore pressure at the center of the globally undrained sphere. The thermal responses shown in Figure 8(a) indicate that the stabilization procedure does not lead to significant changes in thermal responses. The hydraulic responses exhibited in Figure 8

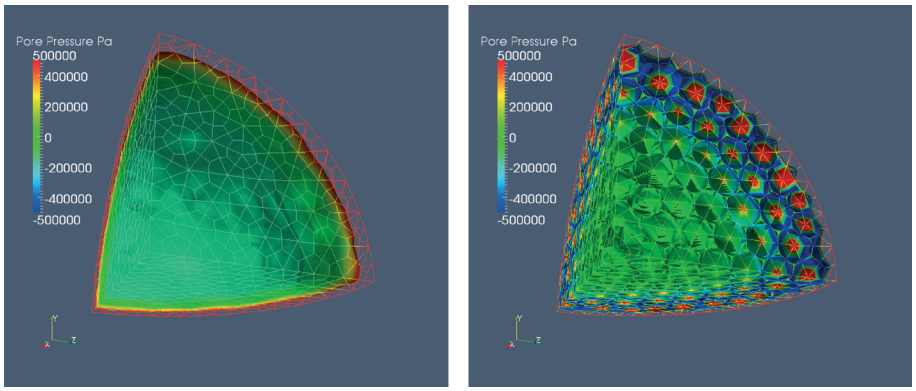

(a) Stabilized FEM response (b) Standard FEM response

Figure 6. Pore pressure profile of undrained porous sphere in heat bath: (a) stabilized FEM response and (b) standard FEM response.

DOI: 10.1002/nme

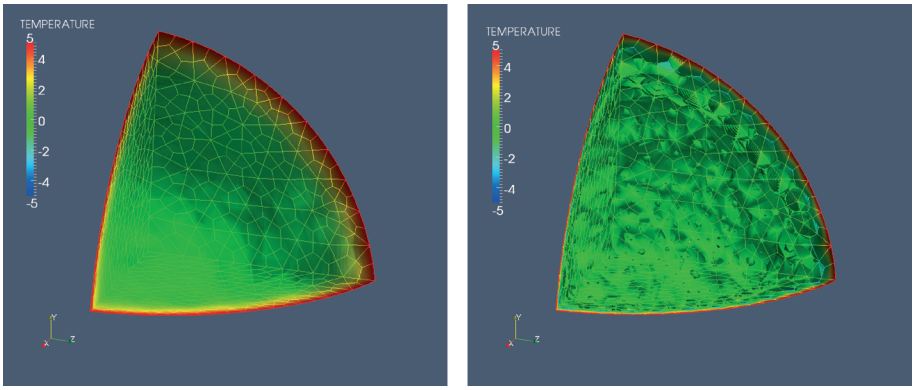

(a) Stabilized FEM response (b) Standard FEM response

Figure 7. Temperature profile of undrained porous sphere in heat bath: (a) stabilized FEM response and (b) standard FEM response.

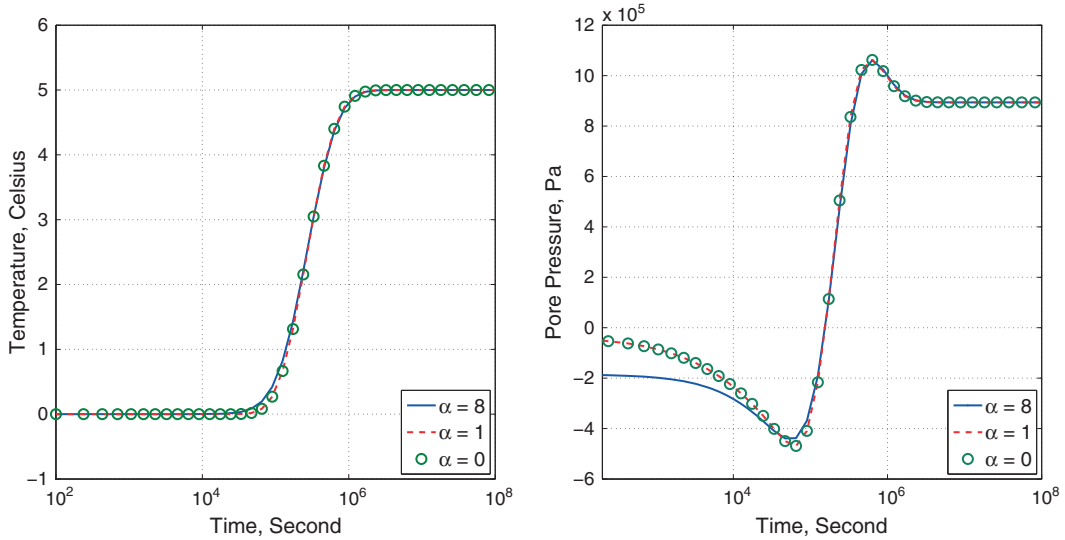

(a) Temperature at Center (b) Pore Pressure at Center

Figure 8. Time-history of the (a) temperature and (b) pore pressure at the center of the undrained sphere. The stabilization parameter equals to 0 (green dot), 1 (red dash line), and 8 (blue line).

indicate that a large stabilization parameter may alter the simulated hydraulic responses at the undrained limit and steady responses are not significantly affected by the stabilization procedure. Figure 9 shows the surface displacement obtained with different stabilization parameters. Again, we note that the discrepancies among standard and stabilized responses are insignificant in the transient and steady state regimes. The results presented in this example indicate that the stabilization procedure is able to eliminate spurious oscillations even when permeability is very low. Nevertheless, over-diffusion may occur if the stabilization parameter assigned in the simulations is larger than the optimal value. The rough estimation of the optimal value described in Section 3.4.3 seems to be working for this particular problem. However, the optimal value of stabilization parameters is usually problem-dependent, and its determination should be done with caution.

To study how the selection of stabilization parameters affects the convergence rate, we conduct additional simulations with stabilization parameter $\alpha = 0, 1, 10$, and 100. Table II shows the residual norms of the Newton–Raphson algorithm taken at the first time step when the undrained sphere has just been put into the heat bath. The residual norms of the trial step and the first four iteration steps are recorded. The numerical experiment indicates that while increasing the value

DOI: 10.1002/nme

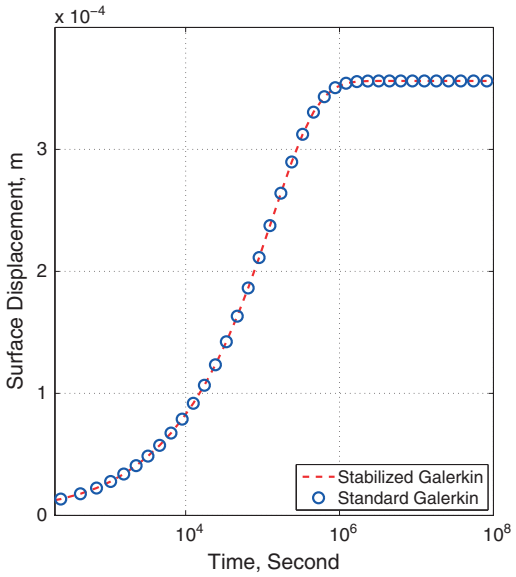

Figure 9. Radial displacement of the boundary of the undrained sphere. The stabilization parameter equals to 0 (green dot), 1 (red dash line), and 8 (blue line).

Table II. Residence norm (square root of the inner product of residual column vector) of the heated undrained sphere simulations at the first four iteration steps.

	$\alpha = 0$	$\alpha = 1$	$\alpha = 10$	$\alpha = 100$
Trial step	5.911e−01	5.911e−01	5.911e−01	5.911e−01
Iteration 1	2.168e+01	4.446e+01	1.049e+02	1.538e+02
Iteration 2	4.058e−03	1.559e−02	6.413e−02	1.099e−01
Iteration 3	2.075e−10	2.349e−10	1.495e−09	3.720e−09
Iteration 4	1.327e−10	1.316e−10	1.323e−10	1.426e−10

of stabilization parameter α does lead to noticeable higher residual at the first two iterations, the convergence rate is not severely affected by the choice of the stabilization parameter.

5.2. *Biaxial undrained compression test with insulated boundaries*

The second example deals with the simulation of a biaxial undrained compression test. Our goal here is to demonstrate that the nonlinear coupling effect, as depicted in Figure 4, has been fully implemented in the finite element model and to assess how the coupling mechanism evolves before and after the shear band is formed.

A rectangular sample of homogeneous thermo-sensitive elasto-plastic material of 4 cm × 1 cm × 14 cm is subjected to a prescribed vertical displacement on the top surface of the specimen, while the bottom of the specimen is fixed. The loading rate is −1.4 cm/hour and the vertical displacement remains constant after reaching −1.4 cm. The specimen is globally undrained and thus no-fluid-flux boundary conditions are prescribed at all six surfaces. To simplify the problem, gravity is neglected for this small specimen, and we also assumed that no phase transition occurred in both the fluid and solid constituents. The temperature is initially uniform at ambient value (zero degree). All six surfaces are thermally insulated and thus no-thermal-flux condition applied to these surfaces. In other words, both the pore pressure and temperature fields have no corresponding Dirichlet boundary condition. To control where the shear band initiates, the right-hand side of the specimen is tapered at $z = 7$ cm, as shown in Figure 10. The material parameters used to conduct these simulations are listed in Table III.

DOI: 10.1002/nme

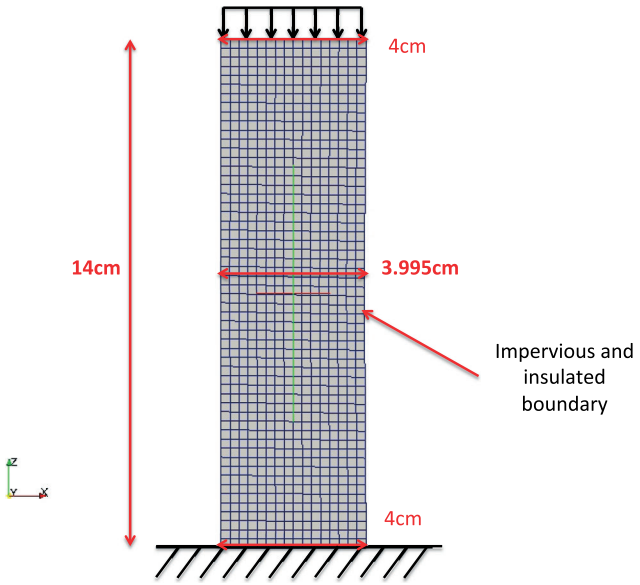

Figure 10. Description of the geometry, boundary, and loading conditions of the biaxial compression problem.

Table III. Material properties of the specimen in non-isothermal condition.

Parameter	Description	Value	Unit
E	Young's modulus	2000	MPa
ν	Poisson's ratio	0.30	Dimensionless
σ_Y	Initial yield strength	100	MPa
$\partial\sigma_Y/\partial\theta$	Thermal hardening parameter	-1.60	MPa/°C
H	Mechanical hardening modulus	0	MPa
T_o	Reference temperature	0	°C
α_s	Skeleton thermal expansion	8.3×10^{-6}	1/°C
α_f	Pore-fluid thermal expansion	6.9×10^{-6}	1/°C
ρ_s	Solid constituent density	2700	kg/m^3
ρ_f	Fluid constituent density	1000	kg/m^3
c_s	Solid specific heat	1700	J/kg/°C
c_f	Fluid specific heat	4200	J/kg/°C
k_θ^s	Solid thermal conductivity	1.00	W/m/°C
k_θ^f	Fluid thermal conductivity	100.00	W/m/°C
K_s	Solid grain bulk modulus	50	GPa
K_f	Fluid bulk modulus	20	GPa
k_o	Kozeny–Carmen coefficient	1×10^{-17}	m/s
μ	Viscosity	1.0×10^{-3}	Pa·s
ϕ^f	Initial porosity	0.25	Dimensionless

One key departure of this numerical example from previous work on THM is that it takes account of the plastic dissipation in the balance of energy equation. For the von Mises J2 plasticity with no mechanical hardening, the thermomechanical dissipation D_{mech} reads [47],

$$D_{\text{mech}} = \sqrt{\frac{2}{3}}\dot{\epsilon^p}\left[\sigma_Y(\theta) - \theta\frac{\partial\sigma_Y(\theta)}{\partial\theta}\right], \tag{5.2}$$

where ϵ^p is the equivalent plastic strain, $\partial\sigma_Y\theta/\partial\theta$ is the thermal softening coefficient, and σ_Y is the flow stress, which corresponds to the Mises yield criterion,

DOI: 10.1002/nme

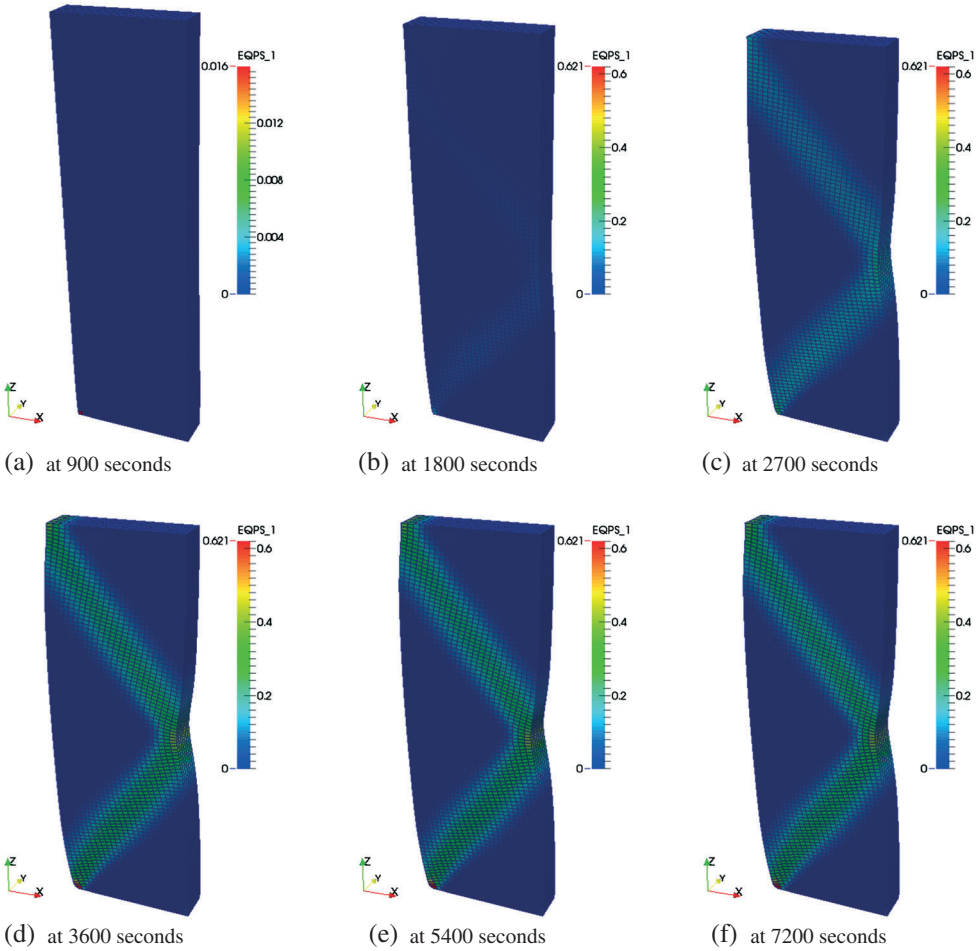

(a) at 900 seconds (b) at 1800 seconds (c) at 2700 seconds

(d) at 3600 seconds (e) at 5400 seconds (f) at 7200 seconds

Figure 11. Equivalent plastic strain (EQPS) at various time during the biaxial loading test at (a) 900, (b) 1800, (c) 2700, (d) 3600, (e) 5400, and (f) 7200 s.

$$||\mathrm{dev}[\boldsymbol{\tau}']|| - \sqrt{\frac{2}{3}}\sigma_Y \leqslant 0 \;\; ; \;\; \boldsymbol{\tau}' = \boldsymbol{P}' \cdot \boldsymbol{F}^T \; . \tag{5.3}$$

5.2.1. Solid responses. The mechanical response is influenced by the pore-fluid trapped inside the specimen and the thermal diffusion. Nevertheless, because there is no heat source in the boundary, the thermal effect on the mechanical response is insignificant. Figure 11 shows the spatial distribution of equivalent plastic strain at various time during the biaxial loading test. We found that plastic strain first initiates at the left lower corner of the specimen at around 900 s. The region with plastic strain enlarges between 900 and 3600 s, while a shear band is formed at the defect point. After 3600 s of simulation, the vertical displacement is held between 3600 and 7200 s, and the plastic strain distribution remains almost identical.

Because the bulk moduli of the solid and fluid constituents are both one order higher than the bulk modulus of the solid skeleton, the global undrained response of the material is expected to be nearly isochoric if the specimen is under the isothermal condition. Nevertheless, as the thermo-hydro-mechanical simulation is run under the non-isothermal condition, the solid skeleton may expand or shrink because of temperature change. This temperature change is due to the mechanical plastic work that converts into heat. The heat in return causes expansion of the solid skeleton. Figures 12 and 13 show the Jacobian of the deformation gradient $\det \boldsymbol{F}$ and the (Eulerian) porosity ϕ^{f} of the solid skeleton at different times during the biaxial loading. Because of the globally undrained status, both the Jacobian and porosity do not change much before the onset of plastic yielding and shear

DOI: 10.1002/nme

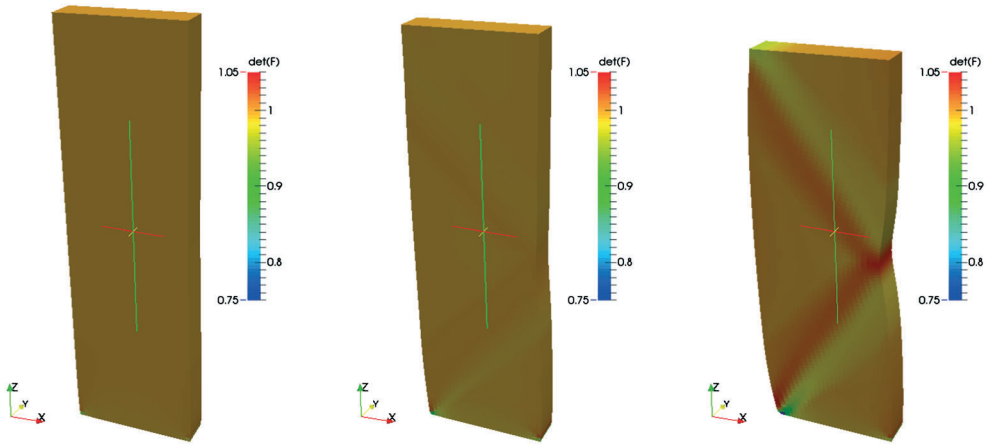

(a) at 900 seconds (b) at 1800 seconds (c) at 3600 seconds

Figure 12. Determinant of the deformation gradient at various time during the biaxial loading test at (a) 900, (b) 1800, and (c) at 3600 s.

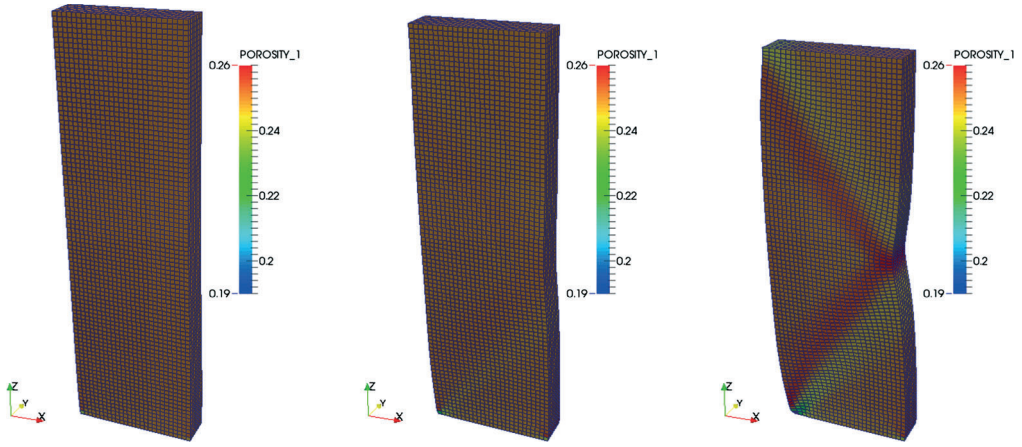

(a) at 900 seconds (b) at 1800 seconds (c) at 3600 seconds

Figure 13. Porosity at various time during the biaxial loading test at (a) 900, (b) 1800, and (c) 3600 s.

band as shown in Figures 12(a) and 13(a). This nearly incompressible response also indicates that structural heating has negligible influence on temperature for this particular simulation. On the other hand, the solid skeleton exhibits a noticeable volumetric expansion/contraction pattern inside the shear band at 3600 s after the vertical loading is prescribed. We record the maximum and minimum of the Jacobian changing from 1 to 1.05 and 0.76, respectively, while the maximum and minimum of the porosities also change 0.25 to 0.26 and 0.19, respectively, after the shear band is formed, as shown in Figures 12(c) and 13(c). This pattern is located at the region where plastic deformation is concentrated (as shown in Figure 11). Because of the coupling of the thermo-hydro-mechanical processes, this plastic work inside the shear band may trigger multiple deformation mechanism. For instance, the plastic work that converted into heat may cause volumetric expansion of both the solid and fluid constituents, but also lead to the shrinkage of the yield surface in stress space and more plastic strain to be accumulated. Meanwhile, as porosity changes because of the thermal effect, both the thermal and hydraulic diffusivities also change accordingly.

5.2.2. Heat transfer. Because the surface of the specimen is thermally insulated, the temperature increase in the specimen is due to the structural heating and plastic dissipation. Figure 14 shows how temperature distributes in the specimen during the ramp-and-hold loading. We observe that

DOI: 10.1002/nme

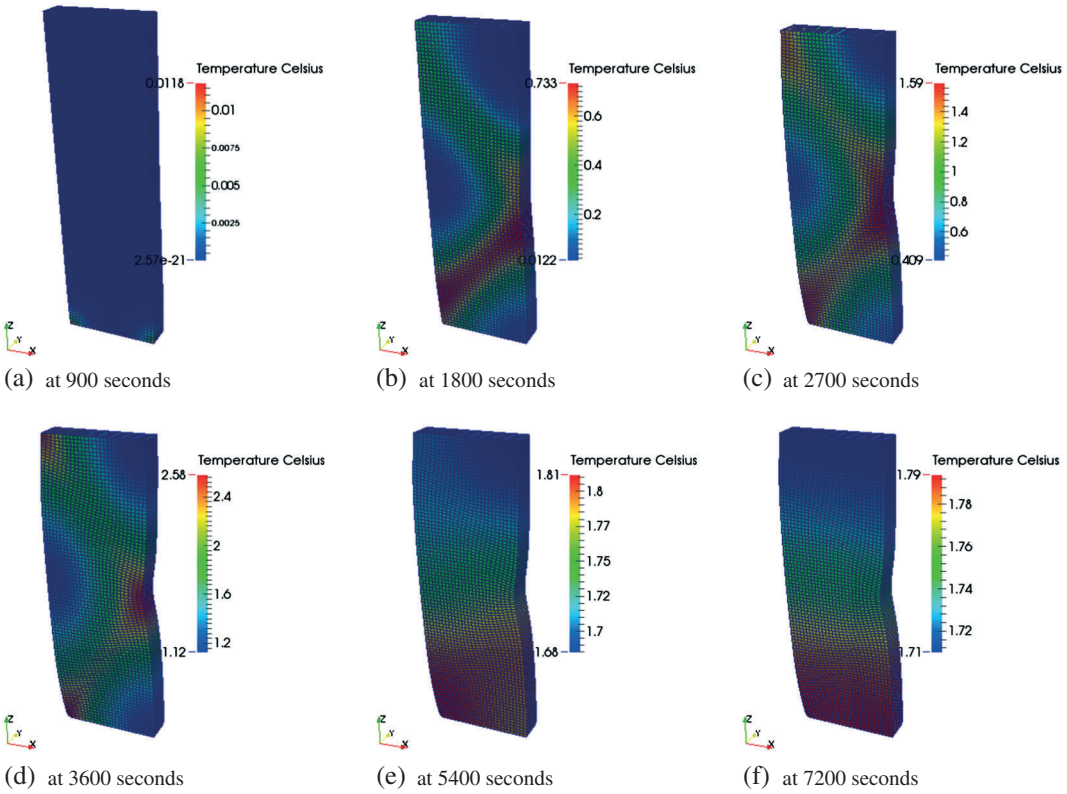

(a) at 900 seconds (b) at 1800 seconds (c) at 2700 seconds

(d) at 3600 seconds (e) at 5400 seconds (f) at 7200 seconds

Figure 14. Temperature at various time during the biaxial loading test at (a) 900, (b) 1800, (c) 2700, (d) 3600, (e) 5400, and (f) 7200 s.

temperature first raised in the plastic zone, as the vertical displacement is accumulating between $t = 0$ and $t = 3600$ s. The heat generated by the plastic work then transfers in the solid specimen through two mechanisms, the convection due to pore fluid transport and the thermal diffusion. In this particular simulation, the effective permeability is very low (10×10^{-19} m/s), and thus the heat transfer process is dominated by the thermal diffusion. As a result, temperature first raised in the region where plastic strain initiated, while the thermal boundary layer gradually propagates. As shown in Figure 14, the thermal diffusion continues when no more displacement is prescribed between $t = 3600$ and $t = 7200$ s. Because the equivalent plastic strain becomes stable at this phase, the heat source vanishes and the spatial gradient of temperature reduces. In particular, the maximum and minimum temperature changes from 2.28 and 1.12°C at $t = 3600$ s to 1.79 and 1.71°C at $t = 7200$ s.

5.2.3. Pore-fluid flow. The pore-fluid inside the specimen is trapped inside the specimen due to the no-flux boundary condition. Figure 15 shows how pore pressure distributes during the ramp-and-hold loading. Because of the low permeability of the specimen, the excess pore pressure easily builds up in the specimen between $t = 0$ and $t = 3600$ s because of the solid skeleton deformation. While this excess pore pressure may dissipate, the low permeability of the specimen and the globally undrained boundary condition may both cause the pore pressure taking longer time to reach steady state. As a result, the pore pressure at the end of the simulations remains less evenly distributed than the temperature. Furthermore, because of the thermal effect on the solid and fluid constituents, temperature may affect the amount of excess pore pressure accumulated in the pores. By comparing Figure 15 with Figure 14, we notice that the hotter region generally has higher pore pressure, although the distributions of pore pressure and temperature do not resemble the same pattern.

DOI: 10.1002/nme

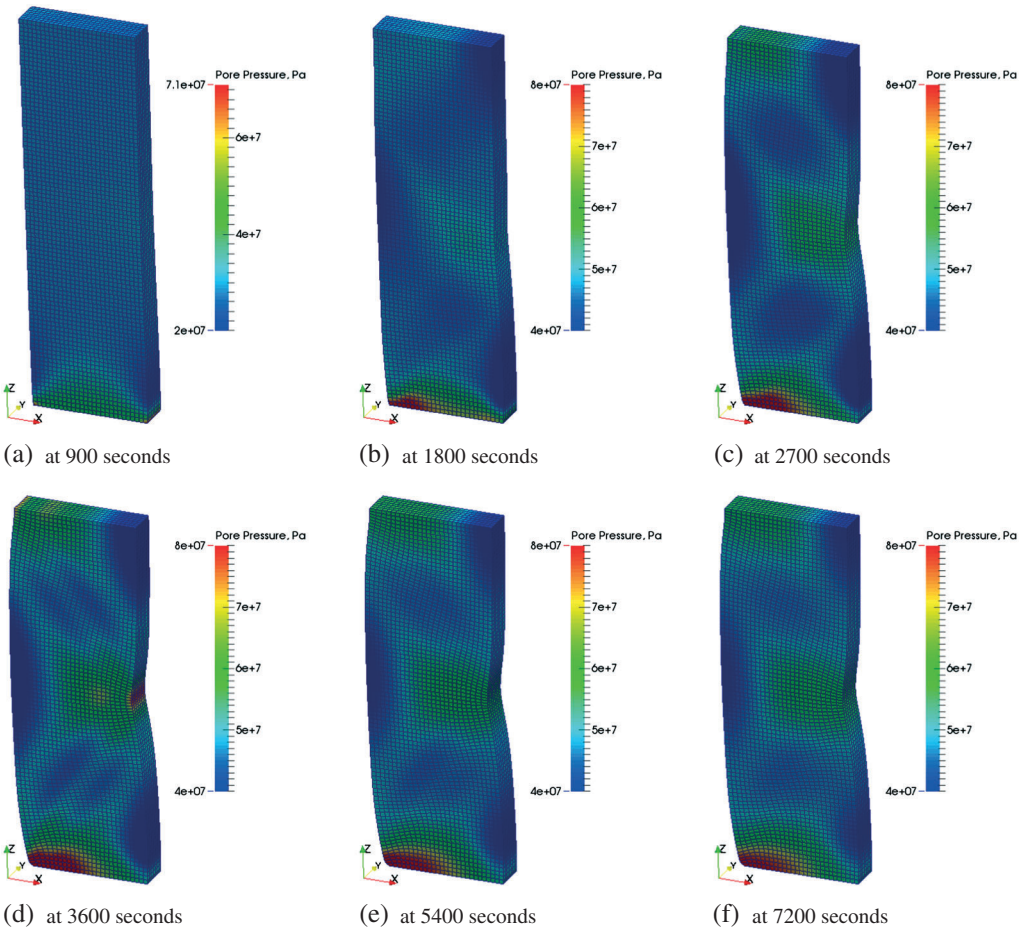

(a) at 900 seconds (b) at 1800 seconds (c) at 2700 seconds

(d) at 3600 seconds (e) at 5400 seconds (f) at 7200 seconds

Figure 15. Pore pressure at various time during the biaxial loading test at (a) 900, (b) 1800, (c) 2700, (d) 3600, (e) 5400, and (f) 7200 s.

5.2.4. Refinement study. To assess the mesh sensitivity of the thermo-hydro-mechanical responses, a mesh refinement study is conducted. Figure 16 shows the three meshes obtained from subdivision refinement. The total number of the finite elements are 448, 3584, and 28 672 accordingly. Figure 17 shows the equivalent plastic strain accumulated in the three finite element meshes at the end of the simulation. While the plastic zone remains very similar to all three meshes, it is clear that the finer mesh tends to accumulate higher plastic strain in the shear band. This mesh dependence is different than the dynamics simulation of isothermal porous media in [75] where equivalent plastic strain is relatively insensitive to the mesh refinement, even though shear band width is found to be narrower in fine meshes. The porosity, which depends on the the volumetric deformation, temperature, and pore pressure, also exhibits mesh dependence as shown in Figure 18.

Presumably, both thermo-mechanical and hydro-mechanical coupling effects may both introduce rate-dependence on the mechanical responses. Nevertheless, the results demonstrated in Figure 17 indicate that this induced rate-dependence is not sufficient to regularize the problem in the transient case. Mesh dependence is also observed in the temperature and pore pressure distribution, as shown in Figures 19 and 20, respectively. The temperature of the shear band in the fine mesh is found to be higher. This is mainly attributed to the fact that temperature increases inside the plastic strain are caused by plastic dissipation. On the other hand, the pore pressure is not concentrated in the shear band as shown in Figure 20. The pore pressure distributions of all three meshes look similar, except at the corners where pore pressure tends to be lower at coarser mesh.

Figure 21 shows the time-history of the temperature and pore pressure at the lower left corner of the specimen. Interestingly, plastic deformation seems to play a significant role on the evolution

DOI: 10.1002/nme

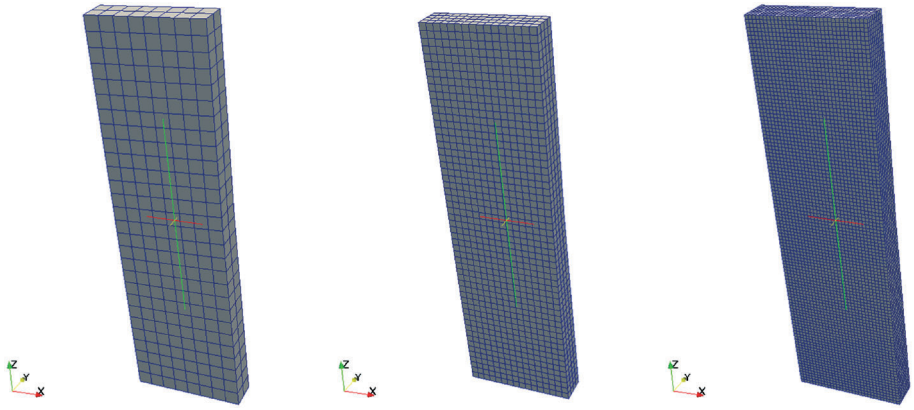

(a) Coarse Mesh (b) Medium Mesh (c) Fine Mesh

Figure 16. Meshes used in refinement study: (a) coarse, (b) medium, and (c) fine.

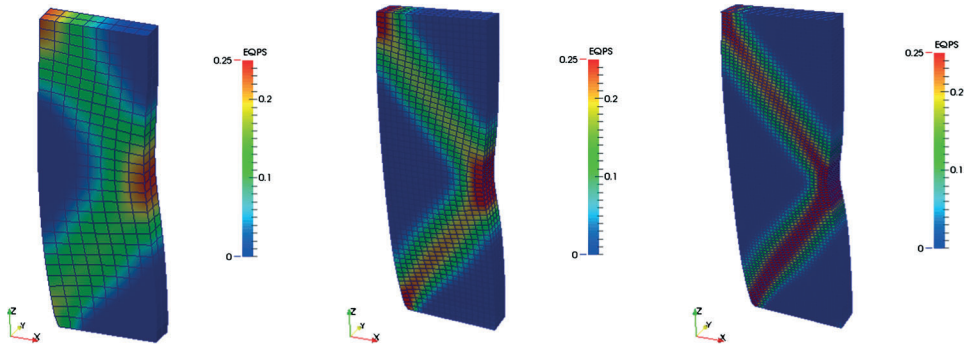

(a) Coarse Mesh (b) Medium Mesh (c) Fine Mesh

Figure 17. Equivalent plastic strain at $t = 7200$ s in three meshes: (a) coarse, (b) medium, and (c) fine.

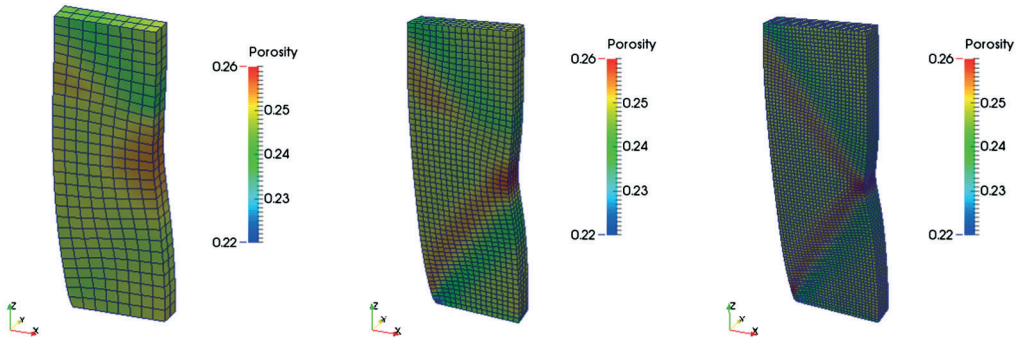

(a) Coarse Mesh (b) Medium Mesh (c) Fine Mesh

Figure 18. Porosity at $t = 7200$ s in three meshes: (a) coarse, (b) medium, and (c) fine.

of both pore pressure and temperature. In particular, temperature at the lower left corner is almost unchanged before the yielding. After the yielding, temperature keeps raising until the prescribed vertical displacement increment stops at 3600 s. While pore pressure begins to increase right after the simulation begins, the onset of plastic yielding leads to a sudden drop of pore pressure followed by another monotonic increase in pore pressure. Both temperature and pore pressure gradually decrease when vertical displacement holds still from $t = 3600$ to 7200 s.

DOI: 10.1002/nme

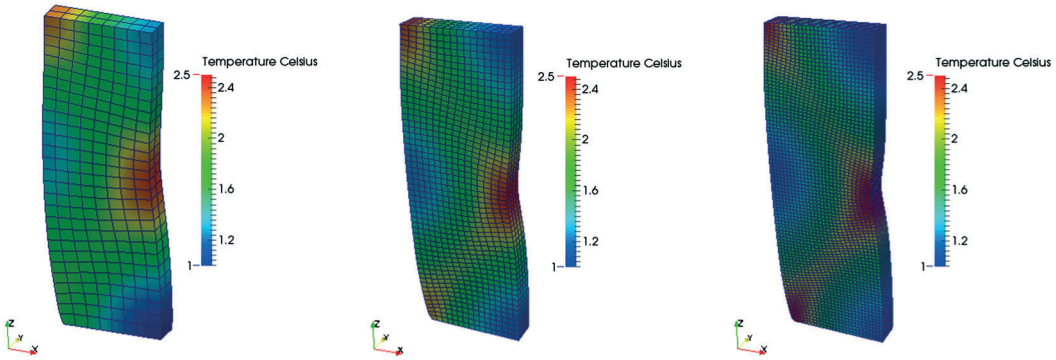

(a) Coarse Mesh (b) Medium Mesh (c) Fine Mesh

Figure 19. Temperature at $t = 7200$ s in three meshes: (a) coarse, (b) medium, and (c) fine.

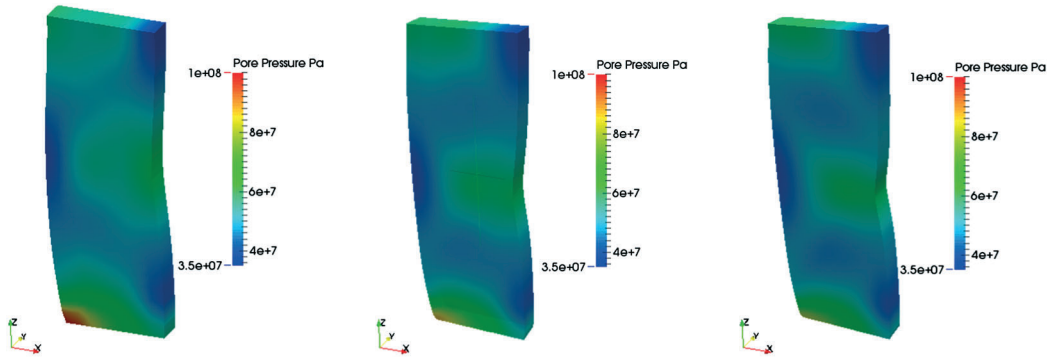

(a) Coarse Mesh (b) Medium Mesh (c) Fine Mesh

Figure 20. Pore pressure at $t = 7200$ s in three meshes: (a) coarse, (b) medium, and (c) fine.

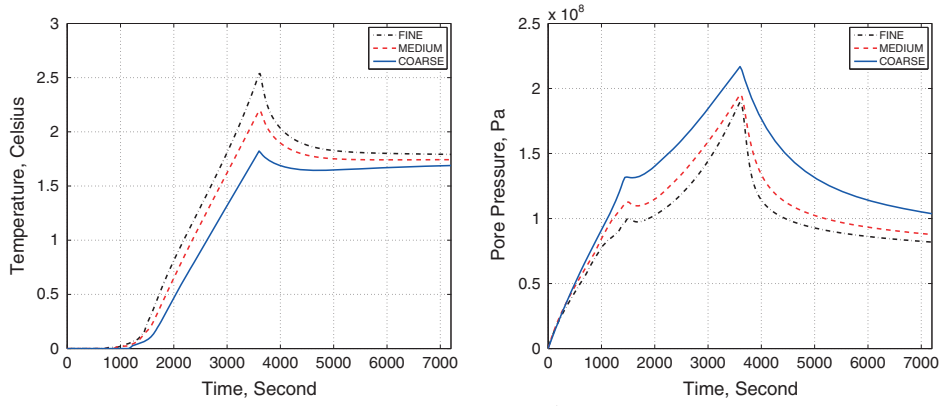

(a) Temperature (b) Pore Pressure

Figure 21. Time histories of (a) temperature and (b) pore pressure at the lower left corner of the three meshes.

Note that refining the mesh seems to have opposite effects on temperature and pore pressure at the corner node. While refining the mesh leads to a lower pore pressure accumulated at the corner, the refinement also causes a higher temperature. The increase of the temperature in finer mesh can be explained by the fact that the power that converts plastic dissipation into heat is higher in finer mesh as evidenced by the higher equivalent plastic strain in the fine mesh shown in Figure 17 when vertical displacement is increasing. Nevertheless, as heat is transferred via both diffusion and

DOI: 10.1002/nme

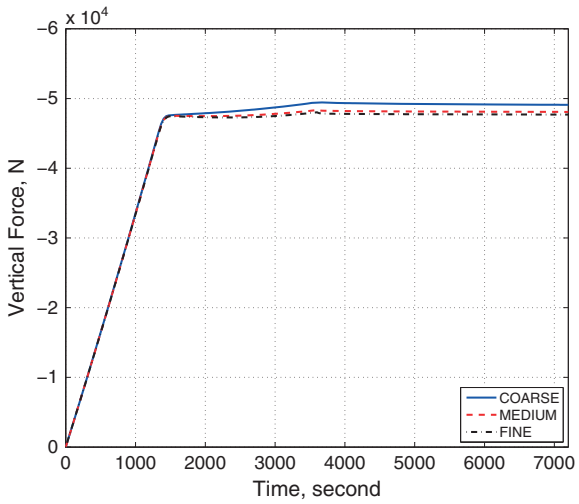

Figure 22. Time-histories of vertical force on the top layer of the specimen.

convection, the initially sharp temperature gradient triggered during the formation of shear band fades over time. At 7200 s after the simulation, the temperature is close to steady state as indicated by the vanishing of sharp temperature gradient shown in Figure 14. This indicates that the mesh dependence of the temperature field is more severe when plastic deformation provides a significant heat source. However, this mesh dependence seems to be more significant when the material is close to adiabatic limit.

On the other hand, we find that pore pressure at the left lower corner is lower in the finer mesh. This observation is different than the isothermal shear band observed in Sun *et al.* [76] where the magnitude and distribution of pore pressure were insensitive to mesh size, even though equivalent plastic strain was also found to be higher in fine mesh. Furthermore, because the porosity and permeability at the lower left corner are both actually lower in the fine mesh, pore fluid is more likely to be trapped and build up excess pore pressure locally. The fact that the pore pressure drops but does not increase upon refinement therefore indicates that the thermal diffusion process may limit the pore pressure build up.

Figure 22 shows the vertical force applied on the top of the specimen. The force due to the displacement prescribed at the top of the specimen is found to be around -50 kN for the coarse mesh and around -48 kN for the medium and fine meshes. In all three cases, the vertical force is at its peak at 3600 s where the displacement increment stops. In between 3600 and 7200 s, the vertical force drops slightly. By comparing results from different meshes shown in Figures 21 and 22, we conclude that the thermo-hydro-mechanical responses are sensitive to the level of refinement. While the discrepancy of the results seems to be decreased upon each refinement, it is not clear whether the solution will be converged if further refinement takes place.

5.2.5. Thermo-hydro-mechanical coupling effects under undrained condition. As reported in [75], shear band width is influenced by the diffusivity of the pore fluid under isothermal condition. In non-isothermal condition, both pore-fluid and thermal flux may influence mechanical responses of the solid skeleton and vice versa. To determine how thermal and hydraulic diffusivities influence the thermo-hydro-mechanical responses, we conduct a parametric study by varying the permeability and thermal conductivity.

In the first set of tests, we conduct two additional numerical simulations with material parameters listed in Table III, but the thermal conductivities of both constituents are both multiplied by 100 in the first simulation and divided by 100 in the second simulation. Figure 23 demonstrates the temperature at 7200 s after the loading. As expected, the material with lower thermal conductivity reaches higher temperature. The temperature also takes longer time to dissipate. Hence, temperature is higher inside the shear band zone.

DOI: 10.1002/nme

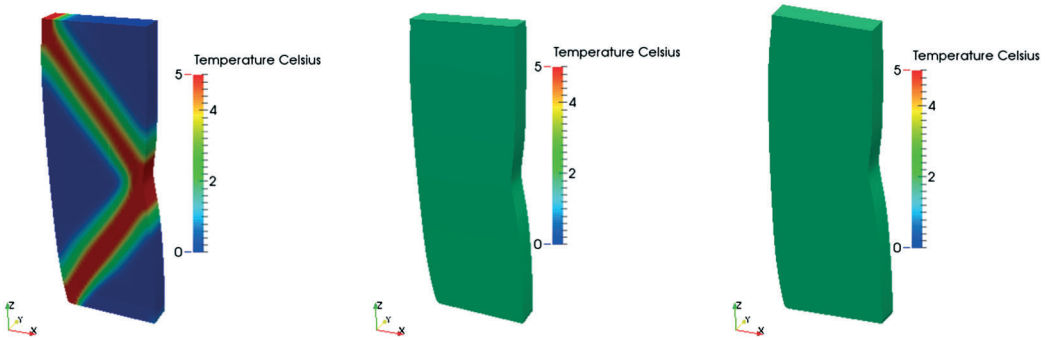

(a) Low Thermal Conductivity (b) Medium Thermal Conductivity (c) High Thermal Conductivity

Figure 23. Temperature profiles at $t = 7200$ s, with initial effective thermal conductivity equals to (a) 0.013, (b) 1.33, and (c) 133W/m/°C. (a) Low thermal conductivity; (b) medium thermal conductivity; and (c) high thermal conductivity.

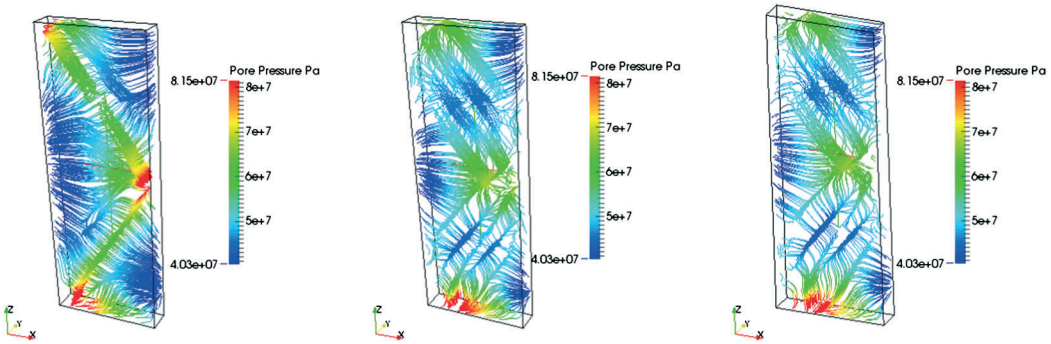

(a) Low Thermal Conductivity (b) Medium Thermal Conductivity (c) High Thermal Conductivity

Figure 24. Flow streamlines at $t = 7200$ s, with initial effective thermal conductivity equals to (a) 0.013, (b) 1.33, and (c) 133W/m/°C. (a) Low thermal conductivity; (b) medium thermal conductivity; and (c) high thermal conductivity.

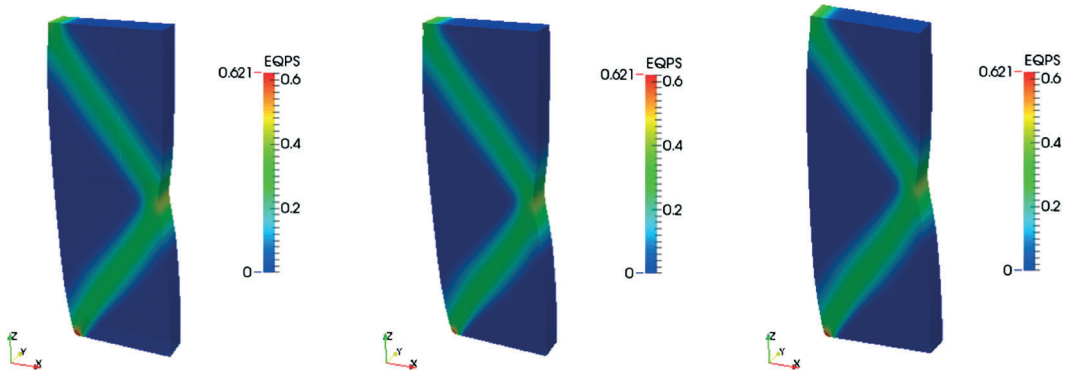

(a) Low Thermal Conductivity (b) Medium Thermal Conductivity (c) High Thermal Conductivity

Figure 25. Equivalent plastic strains at $t = 7200$ s, with initial effective thermal conductivity equals to (a) 0.013, (b) 1.33, and (c) 133W/m/°C. (a) Low thermal conductivity; (b) medium thermal conductivity; and (c) high thermal conductivity.

Interestingly, this higher temperature inside the shear band also influences the hydraulic properties. Figure 24 shows the pore pressure distribution and flow streamlines at 7200 s after the loading. By comparing Figure 23 with 24, one may notice that the pore pressure is higher and more

DOI: 10.1002/nme

concentrated in the shear band in the low thermal conductivity case, even though the initial effect permeability of material are the same in both simulations. Notice that all these features are lost if the heat produced by plastic dissipation is not captured in the balance of energy equation. Varying thermal conductivity nevertheless does not lead to significant changes in the plastic response, as shown in Figures 25 and 26.

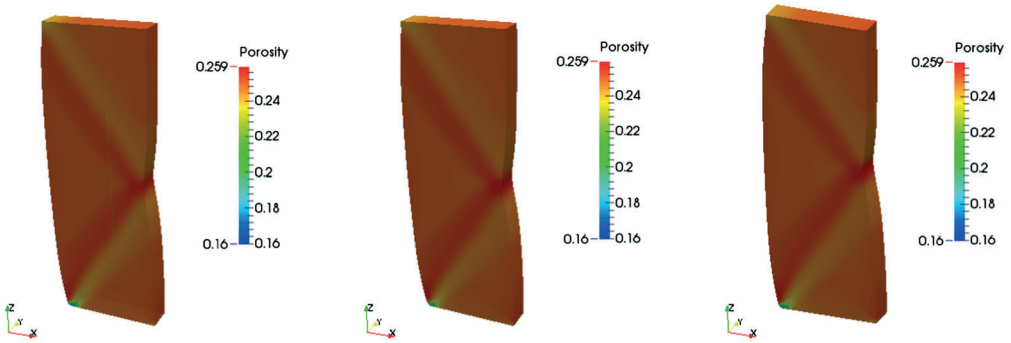

(a) Low Thermal Conductivity (b) Medium Thermal Conductivity (c) High Thermal Conductivity

Figure 26. Porosities at $t = 7200$ s, with initial effective thermal conductivity equals to (a) 0.013, (b) 1.33,and (c) 133W/m/°C. (a) Low thermal conductivity; (b) medium thermal conductivity; and (c) high thermal conductivity.

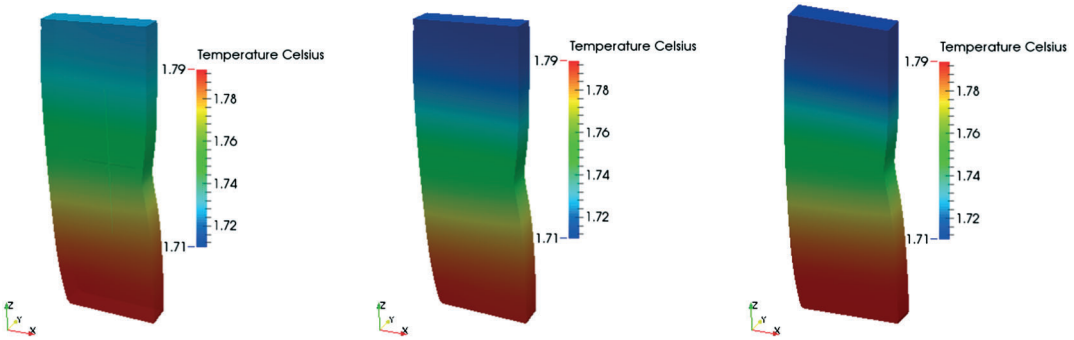

(a) Low Permeability (b) Medium Permeability (c) High Permeability

Figure 27. Temperature profiles at $t = 7200$ s, with permeability coefficient equals to (a) 10^{-16}, (b) 10^{-19},and (c) 10^{-22} m/s. (a) Low permeability; (b) medium permeability; and (c) high permeability.

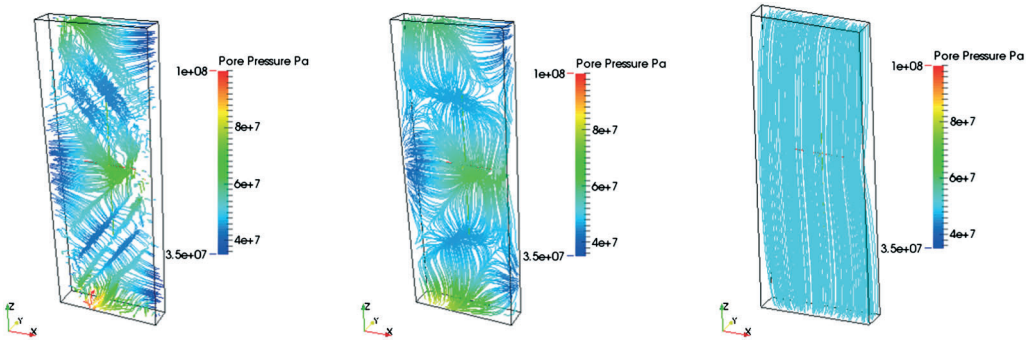

(a) Low Permeability (b) Medium Permeability (c) High Permeability

Figure 28. Flow streamlines at $t = 7200$ s, with permeability coefficient equals to (a) 10^{-16}, (b) 10^{-19}, and (c) 10^{-22} m/s. (a) Low permeability; (b) medium permeability; and (c) high permeability.

DOI: 10.1002/nme

In the second set of tests, we conduct two additional numerical simulations with material parameters listed in Table III, but the Kozeny–Carmen coefficient is changed to 10^{-14} and 10^{-20} m/s, respectively. Figure 27 compares the temperature distribution at the end of the numerical simulations. Even though the material is globally undrained, varying permeability does introduce noticeable changes in temperature. This results indicate the importance of coupling effects. Figure 28 shows the flow streamline obtained form simulations with permeability coefficient equals to (a) 10^{-16}, (b) 10^{-19}, and (c) 10^{-22} m/s. The permeability clearly has a significant impact on both the magnitude of the pore pressure and the flow patterns in the undrained specimen. Interestingly, we found that the plastic responses are not sensitive to changes of permeability and thermal conductivity under the globally undrained and insulated conditions, as shown in Figures 29 and 30.

5.2.6. Convergence rate and stabilization parameters. Finally, additional biaxial compression simulations with $\alpha = 0, 1, 10$, and 100 were conducted to determine whether the value of the stabilization parameter has a noticeable impact on the convergence rate. Table IV shows the residual norms of the Newton–Raphson algorithm taken at the second time step when a small displacement increment is applied on the top of the domain. The residual norms of the trial step and the first four iteration steps are again recorded. The finding is consistent with the results obtained from the heated undrained sphere problem. The numerical experiment again indicates that increasing the value of stabilization parameter α does lead to a slightly higher residuals, but the difference in convergence rate is within an order even when the stabilization parameter α is increased by $10,000\%$.

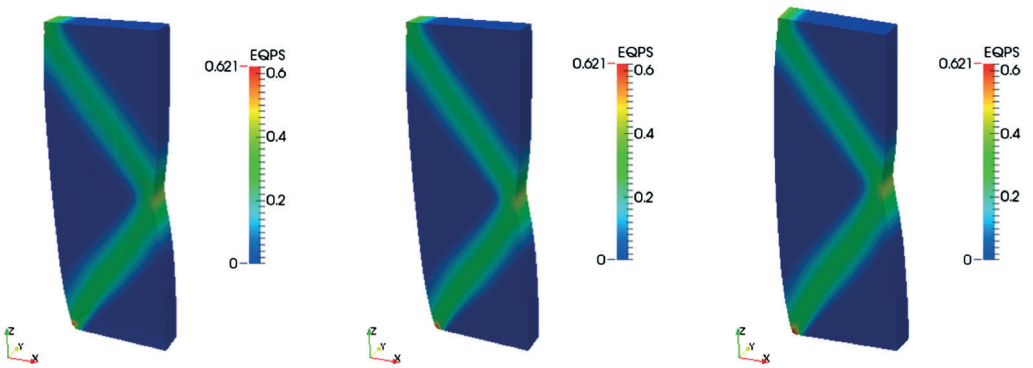

(a) Low Permeability (b) Medium Permeability (c) High Permeability

Figure 29. Temperature profiles at $t = 7200$ s, with permeability coefficient equals to (a) 10^{-16}, (b) 10^{-19}, and (c) 10^{-22} m/s. (a) Low permeability; (b) medium permeability; and (c) high permeability.

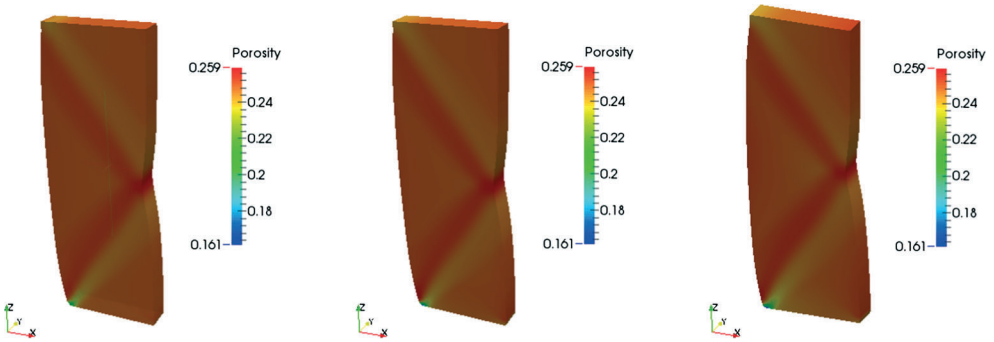

(a) Low Permeability (b) Medium Permeability (c) High Permeability

Figure 30. Temperature profiles at $t = 7200$ s, with permeability coefficient equals to (a) 10^{-16}, (b) 10^{-19}, and (c) 10^{-22} m/s. (a) Low permeability; (b) medium permeability; and (c) high permeability.

DOI: 10.1002/nme

Table IV. Residence norm (square root of the inner product of residual column vector) of biaxial compression simulation at the first four iteration steps.

	$\alpha = 0$	$\alpha = 1$	$\alpha = 10$	$\alpha = 100$
Trial step	7.275e−04	7.275e−04	7.275e−04	7.275e−04
Iteration 1	2.702e−01	2.667e−01	2.634e−01	2.611e−01
Iteration 2	2.735e−07	2.939e−07	3.297e−07	3.649e−07
Iteration 3	8.147e−11	8.139e−11	8.255e−11	1.426e−10
Iteration 4	6.205e−11	6.343e−11	6.525e−11	8.694e−11

Whether one may expect similar trends for all THM boundary value problems remains unknown, but the two numerical experiments seem to suggest that the convergence rate is not very sensitive to the magnitude of the stabilization parameter.

6. CONCLUSION

The new contribution of this work is twofold. First, we establish a large deformation THM theory that fully incorporates the influences of the geometrical nonlinearity on the full coupled solid deformation, pore-fluid diffusion, and heat transfer processes. Using the automatic-differentiation technique to simplify the implementation process, the nonlinear relations between porosity, permeability, and thermal conductivity are fully captured. Secondly, we introduce a stabilized equal-order mixed finite element model that provides stable numerical solutions without over-diffusion. The spatial stability is maintained even when pore-fluid and thermal diffusivities are significantly different. To the best of the author's knowledge, this is the first time the large deformation thermo-hydro-mechanical behavior of porous media is captured with an equal-order finite element in the geometrical nonlinear regime. Our numerical results indicate that such a stabilization procedure is able to eliminate the spurious oscillations even near the undrained and adiabatic limits. Nevertheless, it is acknowledged that the stabilization parameter introduced in this paper may require tuning through trial-and-error. The numerical simulations also exhibit mesh dependence, which indicate that a regularization procedure (e.g., nonlocal scaling [77, 78] and gradient plasticity [79]) is necessary to circumvent the mesh dependence. These shortcomings will be addressed in future studies.

ACKNOWLEDGEMENTS

This research is partially supported by the Earth Materials and Processes program at the US Army Research Office under grant contract W911NF-14-1-0658 and the Provosts Grants Program for Junior Faculty who Contribute to the Diversity Goals of the University at Columbia University. These supports are gratefully acknowledged. The author would like to thank Drs. James W. Foulk III, Alejandro Mota, and Jakob T. Ostien for their encouragement and support to the author during his 3-year tenure at the Sandia National Laboratories. Thanks are also due to Professor Claudio Tamagnini and the author's graduate student Mr. SeonHong Na for reviewing this manuscript, and to the anonymous reviewer for the detailed and constructive remarks.

REFERENCES

1. Coussy O. *Poromechanics*, 2004.
2. McTigue DF. Thermoelastic response of fluid-saturated porous rock. *Journal of Geophysical Research* 1986; **91**(B9):9533–9542.
3. Nguyen T, Selvadurai A. Coupled thermal-mechanical-hydrological behaviour of sparsely fractured rock: implications for nuclear fuel waste disposal. *International Journal of Rock Mechanics and Mining Sciences and Geomechanics Abstracts* 1995; **32**(5):465–479.
4. Li X, Liu Z, Lewis RW. Mixed finite element method for coupled thermo-hydro-mechanical process in poro-elasto-plastic media at large strains. *International Journal for Numerical Methods in Engineering* 2005; **64**(5):667–708.
5. Karrech A, Poulet T, Regenauer-Lieb K. Poromechanics of saturated media based on the logarithmic finite strain. *Mechanics of Materials* 2012; **51**(0):118–136.

DOI: 10.1002/nme

6. Preisig M, Prévost JH. Coupled multi-phase thermo-poromechanical effects. Case study: Co2 injection at in Salah, Algeria. *International Journal of Greenhouse Gas Control* 2011; **5**(4):1055–1064.
7. Kolditz O, Bauer S, Bilke L, Böttcher N, Delfs JO, Fischer T, Görke UJ, Kalbacher T, Kosakowski G, McDermott CI *et al*. Opengeosys: an open-source initiative for numerical simulation of thermo-hydro-mechanical/chemical (THM/C) processes in porous media. *Environmental Earth Sciences* 2012; **67**(2):589–599.
8. Markert B, Heider Y, Ehlers W. Comparison of monolithic and splitting solution schemes for dynamic porous media problems. *International Journal for Numerical Methods in Engineering* 2010; **82**(11):1341–1383.
9. Rutqvist J. Status of the TOUGH-FLAC simulator and recent applications related to coupled fluid flow and crustal deformations. *Computers and Geosciences* 2011; **37**(6):739–750.
10. Jha B, Juanes R. A locally conservative finite element framework for the simulation of coupled flow and reservoir geomechanics. *Acta Geotechnica* 2007; **2**:139–153. DOI: 10.1007/s11440-007-0033-0.
11. Schrefler B. Fe in environmental engineering: coupled thermo-hydro-mechanical processes in porous media including pollutant transport. *Archives of Computational Methods in Engineering* 1995; **2**(3):1–54.
12. Schrefler B, Simoni L, Turska E. Standard staggered and staggered Newton schemes in thermo-hydro-mechanical problems. *Computer Methods in Applied Mechanics and Engineering* 1997; **144**(1):93–109.
13. Sun W, Ostien JT, Salinger AG. A stabilized assumed deformation gradient finite element formulation for strongly coupled poromechanical simulations at finite strain. *International Journal for Numerical and Analytical Methods in Geomechanics* 2013; **37**(16):2755–2788.
14. Goumiri IR, Prévost JH. Cell to node projections: an assessment of error. *International Journal for Numerical and Analytical Methods in Geomechanics* 2011; **35**(7):837–845.
15. Kim J, Wang W, Regueiro RA. Hybrid time integration and coupled solution methods for nonlinear finite element analysis of partially saturated deformable porous media at small strain. *International Journal for Numerical and Analytical Methods in Geomechanics* 2015. DOI: 10.1002/nag.2350.
16. Borja RI. *Plasticity Modeling and Computation*. Springer: Berlin, 2013.
17. Mira P, Pastor M, Li T, Liu X. A new stabilized enhanced strain element with equal order of interpolation for soil consolidation problems. *Computer Methods in Applied Mechanics and Engineering* 2003; **192**(37):4257–4277.
18. Simoni L, Secchi S, Schrefler B. Numerical difficulties and computational procedures for thermo-hydro-mechanical coupled problems of saturated porous media. *Computational Mechanics* 2008; **43**(1):179–189.
19. Truty A, Zimmermann T. Stabilized mixed finite element formulations for materially nonlinear partially saturated two-phase media. *Computer methods in applied mechanics and engineering* 2006; **195**(13):1517–1546.
20. Wan J. Stabilized finite element methods for coupled geomechanics and multiphase flow. *PhD thesis*, 2002. Citeseer.
21. White JA, Borja RI. Stabilized low-order finite elements for coupled solid-deformation/fluid-diffusion and their application to fault zone transients. *Computer Methods in Applied Mechanics and Engineering* 2008; **197**(49): 4353–4366.
22. Zienkiewicz OC, Chan A, Pastor M, Schrefler B, Shiomi T. *Computational Geomechanics with Special Reference to Earthquake Engineering*. Wiley: Chichester, UK, 1999.
23. Babuška I. The finite element method with Lagrangian multipliers. *Numerische Mathematik* 1973; **20**(3):179–192.
24. Bathe KJ. The inf-sup condition and its evaluation for mixed finite element methods. *Computers and Structures* 2001; **79**(2):243–252.
25. Bochev PB, Dohrmann C, Gunzburger M. Stabilization of low-order mixed finite elements for the Stokes equations. *SIAM Journal on Numerical Analysis* 2006; **44**(1):82–101.
26. Brezzi F, Douglas J, Marini LD. Two families of mixed finite elements for second order elliptic problems. *Numerische Mathematik* 1985; **47**:217–235.
27. Borja RI, Tamagnini C, Alarcón E. Elastoplastic consolidation at finite strain part 2: finite element implementation and numerical examples. *Computer Methods in Applied Mechanics and Engineering* 1998; **159**(1):103–122.
28. Dohrmann CR, Bochev PB. A stabilized finite element method for the stokes problem based on polynomial pressure projections. *International Journal for Numerical Methods in Fluids* 2004; **46**(2):183–201.
29. Armero F. Formulation and finite element implementation of a multiplicative model of coupled poro-plasticity at finite strains under fully saturated conditions. *Computer Methods in Applied Mechanics and Engineering* 1999; **171**(3):205–241.
30. Borja RI, Alarcón E. A mathematical framework for finite strain elastoplastic consolidation part 1: balance laws, variational formulation, and linearization. *Computer Methods in Applied Mechanics and Engineering* 1995; **122**(1): 145–171.
31. Nur A, Byerlee J. An exact effective stress law for elastic deformation of rock with fluids. *Journal of Geophysical Research* 1971; **76**(26):6414–6419.
32. von Terzaghi K, Rendulic L. Die wirksame Flächenporosität des Betons. *Zeitschrift des Osterreichischen Ingenieur- und Architekten-Vereines* 1934:1–9.
33. Skempton A. Effective stress in soils, concrete, and rocks. *Selected papers on soil mechanics* 1984:4–16.
34. Cowin SC, Doty SB. *Tissue Mechanics*. Springer: New York, NY, USA, 2009.
35. Biot M. General theory of three dimensional consolidation. *Journal of Applied Physics* 1941; **12**(2):155–164.
36. Rajagopal KR, Tao L. *Mechanics of Mixtures*, Vol. 754. World scientific Singapore: River Edge, NJ, USA, 1995.
37. Holzapfel GA. *Nonlinear solid mechanics: a continuum approach for engineering*, 2000.
38. Rice J, Cleary M. Some basic stress diffusion solutions for fluid-saturated elastic porous media with compressible constituents. *Reviews of Geophysics* 1976; **14**(2):227–241.
39. Bear J. *Dynamics of Fluids in Porous Media*. Elsevier Publishing Company: New York, NY, 1972.

DOI: 10.1002/nme

40. Postelnicu A. Influence of a magnetic field on heat and mass transfer by natural convection from vertical surfaces in porous media considering soret and dufour effects. *International Journal of Heat and Mass Transfer* 2004; **47**(6):1467–1472.
41. Athy LF. Density, porosity, and compaction of sedimentary rocks. *AAPG Bulletin* 1930; **14**(1):1–24.
42. Callari C, Armero F. Analysis and numerical simulation of strong discontinuities in finite strain poroplasticity. *Computer Methods in Applied Mechanics and Engineering* 2004; **193**(27):2941–2986.
43. Coussy O. Revisiting the constitutive equations of unsaturated porous solids using a Lagrangian saturation concept. *International Journal for Numerical and Analytical Methods in Geomechanics* 2007; **31**(15):1675–1694.
44. Selvadurai A, Nguyen TS. Scoping analyses of the coupled thermal-hydrological-mechanical behaviour of the rock mass around a nuclear fuel waste repository. *Engineering Geology* 1997; **47**(4):379–400.
45. Selvadurai A, Suvorov A. Boundary heating of poro-elastic and poro-elasto-plastic spheres. *Proceedings of the Royal Society A: Mathematical, Physical and Engineering Science* 2012; **468**(2145):2779–2806.
46. Jing L, Tsang CF, Stephansson O. Decovalexan international co-operative research project on mathematical models of coupled thm processes for safety analysis of radioactive waste repositories 1995; **32**(5):389–398.
47. Simo J, Miehe C. Associative coupled thermoplasticity at finite strains: formulation, numerical analysis and implementation. *Computer Methods in Applied Mechanics and Engineering* 1992; **98**(1):41–104.
48. Lewis R, Majorana C, Schrefler B. A coupled finite element model for the consolidation of nonisothermal elastoplastic porous media. *Transport in Porous Media* 1986; **1**(2):155–178.
49. Prevost JH. Nonlinear transient phenomena in saturated porous media. *Computer Methods in Applied Mechanics and Engineering* 1982; **30**(1):3–18.
50. Sun W, Andrade J, Rudnicki J. Multiscale method for characterization of porous microstructures and their impact on macroscopic effective permeability. *International Journal for Numerical Methods in Engineering* 2011; **88**(12):1260–1279.
51. Sun W, Andrade JE, Rudnicki JW, Eichhubl P. Connecting microstructural attributes and permeability from 3d tomographic images of in situ shear-enhanced compaction bands using multiscale computations. *Geophysical Research Letters* 2011; **38**(10):1944–8007.
52. Hiroshi H, Minoru T. Equivalent inclusion method for steady state heat conduction in composites. *International Journal of Engineering Science* 1986; **24**(7):1159–1172.
53. Liu R, Wheeler M, Dawson C, Dean R. Modeling of convection-dominated thermoporomechanics problems using incomplete interior penalty Galerkin method. *Computer Methods in Applied Mechanics and Engineering* 2009; **198**(9):912–919.
54. Radovitzky R, Ortiz M. Error estimation and adaptive meshing in strongly nonlinear dynamic problems. *Computer Methods in Applied Mechanics and Engineering* 1999; **172**(1):203–240.
55. Pawlowski RP, Phipps ET, Salinger AG. Automating embedded analysis capabilities and managing software complexity in multiphysics simulation, part I: template-based generic programming. *Scientific Programming* 2012; **20**(2):197–219.
56. Moran B, Ortiz M, Shih C. Formulation of implicit finite element methods for multiplicative finite deformation plasticity. *International Journal for Numerical Methods in Engineering* 1990; **29**(3):483–514.
57. Simo J, Taylor R, Pister K. Variational and projection methods for the volume constraint in finite deformation elastoplasticity. *Computer Methods in Applied Mechanics and Engineering* 1985; **51**(1):177–208.
58. de Souza Neto EA, Perić D, Owen DRJ. *Computational Methods for Plasticity*. John Wiley & Sons, Ltd: West Sussex, United Kingdom, 2008.
59. Wriggers P, Reese S. A note on enhanced strain methods for large deformations. *Computer Methods in Applied Mechanics and Engineering* 1996; **135**(3):201–209.
60. Broccardo M, Micheloni M, Krysl P. Assumed-deformation gradient finite elements with nodal integration for nearly incompressible large deformation analysis. *International Journal for Numerical Methods in Engineering* 2009; **78**(9):1113–1134.
61. Castellazzi G, Krysl P. Patch-averaged assumed strain finite elements for stress analysis. *International Journal for Numerical Methods in Engineering* 2012; **90**(13):1618–1635.
62. Auricchio F, Beirão da Veiga L, Lovadina C, Reali A. A stability study of some mixed finite elements for large deformation elasticity problems. *Computer Methods in Applied Mechanics and Engineering* 2005; **194**(9): 1075–1092.
63. Pantuso D, Bathe KJ. On the stability of mixed finite elements in large strain analysis of incompressible solids. *Finite Elements in Analysis and Design* 1997; **28**(2):83–104.
64. Auricchio F, da Veiga LB, Lovadina C, Reali A, Taylor RL, Wriggers P. Approximation of incompressible large deformation elastic problems: some unresolved issues. *Computational Mechanics* 2013; **52**:1–15.
65. Howell JS, Walkington NJ. Inf–sup conditions for twofold saddle point problems. *Numerische Mathematik* 2011; **118**(4):663–693.
66. Brezzi F, Fortin M. *Mixed and Hybrid Finite Element Methods*. Springer-Verlag New York, Inc.: New York, NY, USA, 1991.
67. Girault V, Raviart PA. *Finite Element Methods for Navier–Stokes Equations, Theory and Algorithms, Volume 5 of Springer Series in Computational Mathematics*. Springer: Berlin, 1986.
68. Tezduyar TE, Osawa Y. Finite element stabilization parameters computed from element matrices and vectors. *Computer Methods in Applied Mechanics and Engineering* 2000; **190**(3):411–430.

DOI: 10.1002/nme

69. Pawlowski RP, Phipps ET, Salinger AG. Automating embedded analysis capabilities and managing software complexity in multiphysics simulation, part I: template-based generic programming. *Scientific Programming* 2012; **20**(2):197–219.
70. Pawlowski RP, Phipps ET, Salinger AG, Owen SJ, Siefert CM, Staten ML. Automating embedded analysis capabilities and managing software complexity in multiphysics simulation, part II: application to partial differential equations. *Scientific Programming* 2012; **20**(3):327–345.
71. Salinger AG, Pawlowski RP, Phipps ET, Bartlett RA, Hansen GA, Kalashnikova I, Ostien JT, Sun W, Chen Q, Mota A, Muller RP, Nielsen E, Gao X. Albany: a component-based partial differential equation code built on Trilinos. *ACM Transactions on Mathematical Software* 2013. Submitted.
72. Heroux MA, Bartlett RA, Howle VE, Hoekstra RJ, Hu JJ, Kolda TG, Lehoucq RB, Long KR, Pawlowski RP, Phipps ET *et al*. An overview of the Trilinos project. *ACM Transactions on Mathematical Software (TOMS)* 2005; **31**(3):397–423.
73. Notz PK, Pawlowski RP, Sutherland JC. Graph-based software design for managing complexity and enabling concurrency in multiphysics PDE software. *ACM Transactions on Mathematical Software (TOMS)* 2012; **39**(1):1.
74. Harari I. Stability of semidiscrete formulations for parabolic problems at small time steps. *Computer Methods in Applied Mechanics and Engineering* 2004; **193**(15):1491–1516.
75. Zhang H, Sanavia L, Schrefler B. An interal length scale in dynamic strain localization of multiphase porous media. *Mechanics of Cohesive-frictional Materials* 1999; **4**(5):443–460.
76. Sun W, Chen Q, Ostien JT. Modeling the hydro-mechanical responses of strip and circular punch loadings on water-saturated collapsible geomaterials. *Acta Geotechnica* 2014; **9**(5):903–934.
77. Bazant ZP, Jirásek M. Nonlocal integral formulations of plasticity and damage: survey of progress. *Journal of Engineering Mechanics* 2002; **128**(11):1119–1149.
78. Sun W, Mota A. A multiscale overlapped coupling formulation for large-deformation strain localization. *Computational Mechanics* 2014; **54**(3):803–820.
79. Fleck N, Muller G, Ashby M, Hutchinson J. Strain gradient plasticity: theory and experiment. *Acta Metallurgica et Materialia* 1994; **42**(2):475–487.

DOI: 10.1002/nme